Multi-Decadal Measurements of UTLS Gravity Waves Derived from Commercial Flight Data

Corwin James Wright[1] and Timothy Paul Banyard[1]

[1]University of Bath

November 24, 2022

Abstract

Gravity waves (GWs) are key drivers of atmospheric dynamics, with major impacts on climate and weather processes. However, they are challenging to measure in observational data, and as a result no large-area multi-decadal GW time series yet exist. This has prevented us from quantifying the interactions between GWs and long-timescale climate processes. Here, we exploit temperatures measured by commercial aircraft since 1994 as part of the IAGOS atmospheric chemistry research programme to produce a novel 26-year time series of upper troposphere/lower stratosphere (UTLS) GW measurements across most of the northern hemisphere. We analyse 90\,342 flight-hours (76.2 million flight-kilometres) of data, typically at a temporal resolution of seconds and with high temperature precision. We show that GW activity in the northern-hemisphere UTLS is consistently strongest north of and above the upper tropospheric jet. We also show that GW sources not typically observed in stratospheric data but assumed in model schemes, such as the Rocky Mountains, are visible at these altitudes, suggesting that wave momentum from these sources is deposited specifically between $\sim$200–50\,hPa. Our data shows no significant impact of the Quasi Biennial Oscillation, the Northern Annular Mode, or climate change. However, we do see strong evidence of links with the El Ni\ no-Southern Oscillation, which modulates the measured GW signal by $\sim$25\%, and weak evidence of links with the 11-year solar cycle. These results have important implications for atmospheric process modelling and for understanding large-scale climate teleconnections.

Multi-Decadal Measurements of UTLS Gravity Waves Derived from Commercial Flight Data

C. J. Wright[1] **and T. P. Banyard**[1]

[1]Centre for Space, Atmospheric and Oceanic Science, University of Bath, Bath, UK

Key Points:

- We exploit in-situ aircraft data from 1994 to date to produce a 26-year UTLS gravity wave dataset
- Northern Hemisphere UTLS GWs show a statistically-significant 25% amplitude change over ENSO cycle
- Strong and consistent GW activity seen above and poleward of the upper tropospheric jet.

Corresponding author: Corwin Wright, c.wright@bath.ac.uk

Abstract

Gravity waves (GWs) are key drivers of atmospheric dynamics, with major impacts on climate and weather processes. However, they are challenging to measure in observational data, and as a result no large-area multi-decadal GW time series yet exist. This has prevented us from quantifying the interactions between GWs and long-timescale climate processes. Here, we exploit temperatures measured by commercial aircraft since 1994 as part of the IAGOS atmospheric chemistry research programme to produce a novel 26-year time series of upper troposphere/lower stratosphere (UTLS) GW measurements across most of the northern hemisphere. We analyse 90 342 flight-hours (76.2 million flight-kilometres) of data, typically at a temporal resolution of seconds and with high temperature precision. We show that GW activity in the northern-hemisphere UTLS is consistently strongest north of and above the upper tropospheric jet. We also show that GW sources not typically observed in stratospheric data but assumed in model schemes, such as the Rocky Mountains, are visible at these altitudes, suggesting that wave momentum from these sources is deposited specifically between ∼200–50 hPa. Our data shows no significant impact of the Quasi Biennial Oscillation, the Northern Annular Mode, or climate change. However, we do see strong evidence of links with the El Niño-Southern Oscillation, which modulates the measured GW signal by ∼25%, and weak evidence of links with the 11-year solar cycle. These results have important implications for atmospheric process modelling and for understanding large-scale climate teleconnections.

1 Introduction

In-Service Aircraft for a Global Observing System (IAGOS) is a European research infrastructure programme designed to observe the upper troposphere and lower stratosphere (UTLS) using instruments fitted as an additional payload to commercial aircraft. IAGOS data are well-validated, and have been used in over 400 scientific studies to date. Including flights operated under the earlier MOZAIC and CARIBIC programmes, the dataset contains >60 000 flights, covering the period from 1994 onwards.

While the primary focus of IAGOS is on atmospheric chemistry, the metadata recorded to contextualise these measurements are also of significant scientific use. These metadata provide a long-term high-resolution record of atmospheric temperatures and winds at small spatial scales, with high precision and good quality control. They have previously been used in a number of dynamical studies (Lindborg, 1999; Cho & Lindborg, 2001; Scott et al., 2001; Skamarock, 2004; Callies et al., 2014, 2016; Berkes et al., 2017; Li & Lindborg, 2018), which have primarily focused on the bulk statistical nature of the data rather than geographically-resolved features, and in particular on the fine structure of horizontal winds.

Here, we exploit these metadata to study geographically-resolved small-scale atmospheric gravity waves (GWs) in temperature data. GWs are near-ubiquitous in the middle and upper atmosphere, and play a vast range of vital dynamical roles, including controlling the stratospheric jets and the large-scale equator-to-pole and pole-to-pole circulations, driving chemical transport and ozone depletion, and acting to help stratospheric clouds form (Murgatroyd & Singleton, 1961; Fritts & Alexander, 2003; M. J. Alexander et al., 2010; S. P. Alexander et al., 2013; Geller et al., 2013). However, due to their small physical scales (at most tens of kilometres and usually much less in the vertical, and tens to hundreds of kilometres in the horizontal) they are technically challenging to measure, and as a result few long GW time series exist.

The challenges of measuring GWs are particularly acute in the UTLS. Ground-based instruments and radiosonde balloons provide limited spatial coverage, particularly over the open ocean, while scientific aircraft and superpressure balloon campaigns are limited in number and coverage and do not take routine measurements. To add to this, the satellite methods that have revolutionised our stratospheric gravity wave knowledge in

the last two decades perform extremely poorly in the UTLS, due to their relatively coarse spatial resolution and the vertical structure of the temperature-tropopause itself, which heavily complicates use of profile-based detrending methods for extracting GW signatures from background variations. As such, IAGOS data can provide a unique long-term window on UTLS GWs, particularly at remote locations.

Callies et al. (2016) applied spectral decomposition methods to MOZAIC wind data from 2002–2010, demonstrating that the data contained signatures consistent with inertia–gravity waves in the lower stratosphere. However, they did not identify such a relationship in the upper troposphere, a conclusion they ascribed to mesoscale variances in measured along-track wind components. Here, we use temperature data from a 1994-2019 superset of IAGOS data; these temperatures do not appear to share the along-track variance issues, and contain clear GW signatures amenable to spectral analysis in both the upper troposphere and lower stratosphere.

In Section 2 we describe the data used, and in Section 3 the analyses performed. Section 4 then examines seasonal maps of the northern hemisphere, considering both directly-measured geophysical variables (i.e. wind and temperature) and our analysis outputs. In Section 5 we study time series for 18 selected regions, which are later tested against multiple climate indices in Section 7, while Section 6 examines the relationship between GWs and the upper-tropospheric jet. Section 8 compares our results to previous UTLS studies of GWs, and Section 9 discusses a key implication of our results. Finally, we discuss systematic biases and deficiencies in our dataset in Section 10, before summarising and drawing conclusions in Section 11.

2 IAGOS Data

We use data from the IAGOS Data Portal (Boulanger et al., 2019), incorporating all final-version recorded flights from the 1st of August 1994, the start of the dataset, to the end of 2019. A significant lag often exists between data being recorded and finalised, and accordingly from October 2017 onwards our dataset does not include all IAGOS flights.

We specifically use aircraft-instrument-derived temperature data ('air_temp_AC'). These data are recorded by the aircraft's standard instrumentation rather than the IAGOS package and thus may be less accurate, but are available for every flight. Using these data approximately doubles available data relative to temperatures measured by the instrument packages alone, with the increase largest in later years.

Since we detrend the data to identify GWs, absolute biases and drifts over long periods of flight are not important to our analysis, thus potentially justifying use of these data. To test this, Figure 1 compares 'air_temp_AC' against three other IAGOS temperature products, computed over all level-flight measurements for which each variable-pair exists in January 2000, detrended and preprocessed as described below. We see close agreement, with correlations of >0.95 and linear fits. There is a bias between stagnation-temperature and direct-temperature products; this bias is symmetric about zero perturbation, and thus will lead to a reduction $\sim$10% in our measured wave amplitudes relative to if stagnation products were used.

Other randomly-tested months were analysed in the same way, with equivalent results.

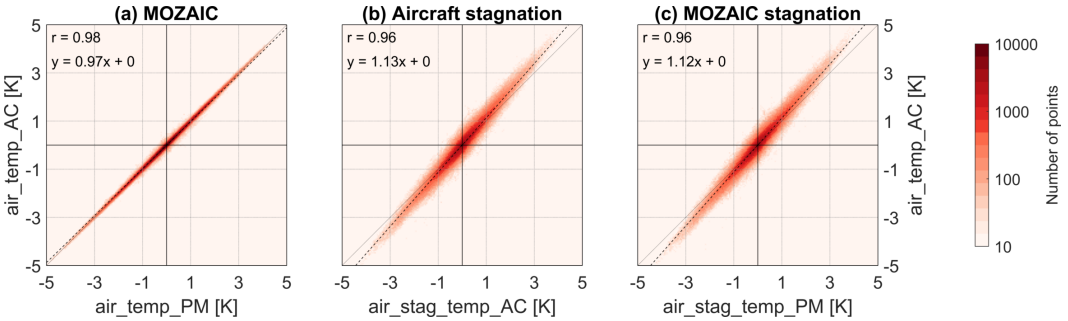

Figure 1. Comparison of perturbations in aircraft-measured temperature ('air_temp_AC') against perturbations in (a) MOZAIC-measured temperature ('air_temp_PM') (b) aircraft-measured stagnation temperature ('air_stag_temp_AC') and (c) MOZAIC-measured stagnation temperature ('air_stag_temp_PM') for corresponding measurements in each dataset for the month of January 2000. Each panel shows a scatter-density plot of (vertical axis) 'air_temp_AC' against (horizontal axis) each other product, with a bin size of 0.05 K on each axis. Close agreement is seen, justifying use of the aircraft-measured temperature data for our GW analyses.

3 Methods

3.1 Preprocessing of IAGOS Data

IAGOS data include ascents and descents as well as level cruising. The data also vary in resolution and occasionally include minor errors. As such, some preprocessing is required to provide consistent data for analysis.

We first apply all error flags, removing data entirely if any variable we subsequently use is flagged as bad. After this, some records contain either negative timesteps or repeated latitude/longitude pairs. For these records, we re-order the data to ascend monotonically in time and replace duplicated pairs via linear interpolation.

We next split the data into sections of straight near-level flight, removing any parts where height or direction changes quickly. These include ascents and descents, which we do not use. We label these straight stable sections as "cruises", which we define as having barometric altitude changes of <100 m and directional changes of <45° within any rolling fifteen-minute time window. The first check ensures we measure a consistent physical regime, while the latter check is to avoid potential measuring a laminar feature twice at different angles and misidentifying it as a wave. Each cruise is subsequently analysed independently.

We then linearly interpolate the data to a 1 km along-track resolution. This is representative of the original data, which have a mean spacing of 1.09 km (median 1.01 km, standard deviation 0.50 km). We discard any cruises with discontinuities greater than 20 km, linearly interpolating over gaps smaller than this. We then remove cruises which, after these steps, are <1000 km long. After additional removal of out-of-band data (Section 3.2), we are left with 76.2 million data points, distributed as shown in Figure 2 and representing 90 342 flight-hours of data. Our data are biased towards the northern hemisphere, especially the northern Atlantic Ocean, and skew towards higher altitudes in later years. We divide the data into three pressure bands (>225 hPa, 225-205 hPa and <205 hPa respectively) to contextualise relative coverage as a function of height; these bands are chosen to split the data into three approximately equal subsets, rather than on the basis of physical differences, and are not used below.

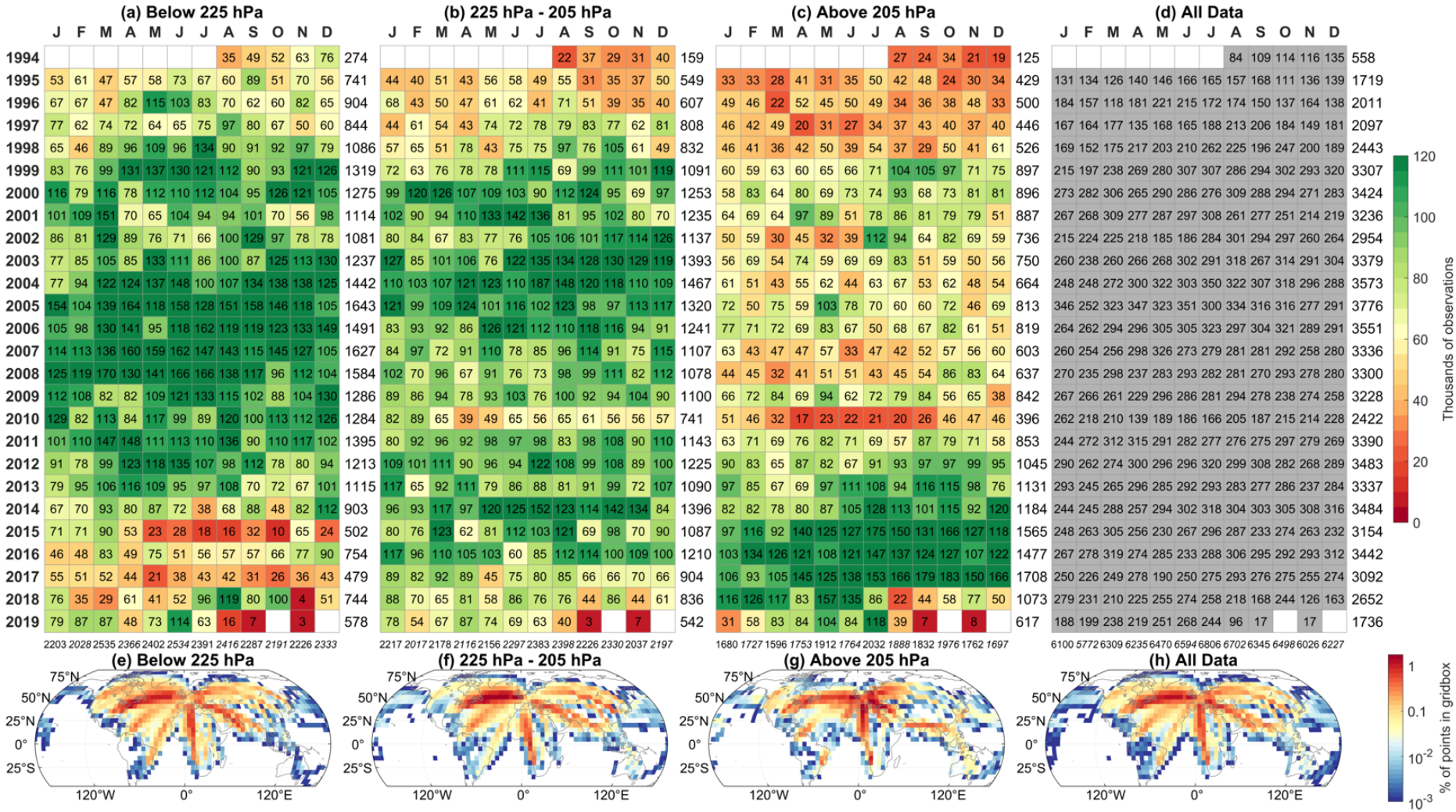

Figure 2. Data points available for our analysis after filtering, distributed in (a-d) time and (e-h) space, and subdivided into (a,e) vertically below 225 hPa (b,f) 225 hPa – 205 hPa (c,g) vertically above 205 hPa and (d,h) all data. These height bands are chosen purely to provide a roughly even split, and have no especial physical significance. Numerical values in (a-d) are in thousands of data points, with column (row) totals shown at the end of the column (row). Values in (e-h) are as a percentage of the global total in that height range, using $3° \times 3°$ bins.

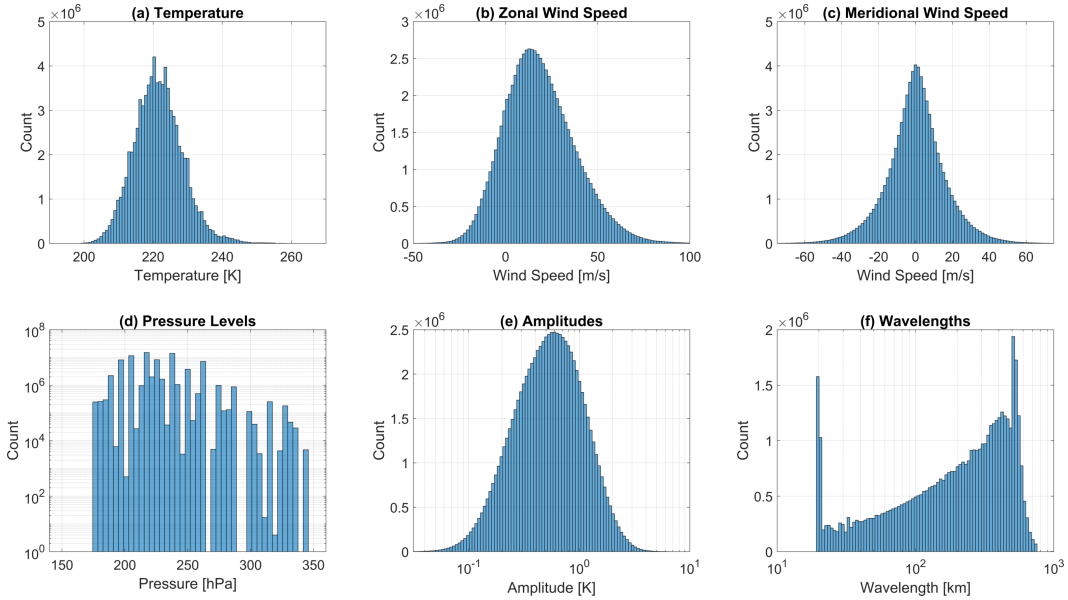

Figure 3. Histograms of basic data properties, integrated across the entire dataset. (a-d) show directly measured temperature, zonal wind speed, meridional wind speed and pressure. (e) and (f) show derived wave amplitudes and wavelengths.

Figures 3a-d show the broad characteristics of the resulting dataset. Temperatures and zonal winds show smooth distributions with positive skew, while meridional winds show a near-symmetric distribution focused around zero. Pressures show a spiky distribution (note the logarithmic ordinate), consistent with preferred flight levels.

3.2 Gravity Wave Analysis

To identify GWs, we use a one-dimensional Stockwell Transform (ST) method. Such methods have been widely used in previous GW research (e.g. M. J. Alexander et al., 2008; Wright et al., 2010; Hindley et al., 2015; Moss et al., 2016), and allow us to localise measured GWs in both location and wavenumber.

We first smooth each cruise with a 900 km second-order Savitzky-Golay filter, and subtract this from the original data to produce perturbation series. Figure 6 of Hindley et al. (2015) shows the transfer function for this filter, which here provides good transmittance up to ∼500 km, dropping off sharply above this. Callies et al. (2014) saw a change in horizontal dynamical scales at ∼500 km, supporting this choice. We then spectrally analyse each cruise, using the ST implementation of Hindley et al. (2019). From this we estimate wave amplitude A and along-flight horizontal wavenumber k for the strongest signal present at each data point (see e.g. M. J. Alexander et al., 2008). We restrict the analysis to wavelengths between 10 km and 600 km.

Figures 3e-f show the resulting amplitudes and wavelengths. Both distributions are smooth, with amplitudes centred at 0.7 K and wavelengths peaking at 500 km. A maximum is seen in the lowest two wavelength bins at ∼20 km, arising from small-scale noise aliased into the analysed range. To prevent this spurious peak contaminating our results, we remove data with wavelengths below 25 km. We also remove wavelengths longer than 500 km, as they will be attenuated by the detrending filter and in any case are expected to be dynamically different. Finally, we remove points with measured wavelengths more than twice the distance between the measurement and the start or end of the cruise; this

reduces edge-truncation effects in our results, but will introduce a short-wavelength bias near the start and end of flights. This effect will be largest over Europe, where most flights commence or terminate. The removed data are distributed approximately evenly across the other distributions in Figure 3, and removing them does not affect their form.

Sensitivity tests suggest our results are only weakly affected by the choice of a 1 km interpolant or the definition of a cruise. The choice of detrending filter also has only a small effect: boxcar, Lanczos and Gaussian filters were also tested, with very little difference for the boxcar or Lanczos and, for the Gaussian, a shift to slightly higher amplitudes and longer wavelengths but with otherwise similar results. However, our results are strongly affected by the 900 km filter length. In particular, tests with significantly longer filters produce large peaks in wavelength over the midpoints of typical long-haul flights, i.e. the mid-Atlantic and central Asia, a bias which is avoided by using our smaller value.

3.3 Cluster Mapping

3.3.1 Hierarchical Cluster Analysis

Due to the uneven distribution of our measurements, balancing the limited data in many regions with dense coverage in others is non-trivial. Using a high-resolution grid leaves large gaps, while a low-resolution grid underrepresents available resolution, leading to the discard of large areas when we later impose a minimum number of measurements per gridbox.

To balance these competing scales, we use an approach combining hierarchical clustering and statistical bootstrapping. This is based on the work of Wright et al. (2012, 2013), and produces maps with good spatial coverage over most of the northern hemisphere, while still exploiting the full resolution where measurement density is high. We carry out this analysis at the seasonal level, using combined data from all years for boreal winter (DJF), spring (MAM), summer (JJA) and autumn (SON) respectively.

We first produce a list of latitude/longitude pairs. To make calculations computationally tractable, we assume that points within the same $0.2^\circ \times 0.2^\circ$ box represent the same location and de-duplicate at this level of precision (this does not affect our results, as the data values are restored once the grid is produced). This reduced dataset still represents the data distribution at scales well above this, and is therefore suitable for cluster generation, since we later impose a minimum area of $0.5^\circ \times 0.5^\circ$.

We next apply a k-means algorithm to the geolocation data, dividing the data into a fixed number of spatially-compact clusters. For each season, we do this 10 000 times, selecting the iteration with the lowest total distance between measurements and cluster centres. We use a Euclidian distance metric in latitude/longitude space - this is strictly incorrect for the Earth, but in practice introduces only a small error at the scale of our clusters, and provides significant runtime benefits.

We initially define 4 000 clusters; this is arbitrary, and is chosen as the highest round number to which we can apply our subsequent bootstrapping analysis in reasonable computer time (hours) and memory (tens of gigabytes) on the system used. Systematically varying this number suggests that using 4 000 clusters gives statistically similar results to maps produced using lower values, but providing finer geographic resolution. Tests using regular latitude-longitude grids instead of the cluster analysis also produce similar results, but without geographically-variable resolution.

We then re-assign each measurement we removed in the de-duplication step to the geographically-closest cluster. Measurements >300 km from a cluster centre are discarded. Finally, we require at least 500 measurements within each cluster, discarding those with fewer and reassigning their data to the next-nearest cluster, while retaining the 300 km

limit. This reduces the number of clusters used to slightly below 4 000 - for example, Figure 4 actually contains 3 764 clusters.

3.3.2 Bootstrap Statistics

Due to the inhomogenous data distribution, this produces clusters which, while representing both large and small scales well, contain uneven numbers of measurements, with a spread of three orders of magnitude in population (compared to five orders of magnitude using a regular 3° grid). While suitable for mapping, this may introduce spurious inter-cluster variations in the statistics we compute, namely the median and Gini's coefficient of concentration G (used previously for GW studies in e.g Plougonven et al., 2012; Wright et al., 2013; Hindley et al., 2019; Kuchar et al., 2020). Means were also calculated for all clusters and showed spatially consistent results but with spike-values in some clusters due to outliers.

To correct for these possible variations, we bootstrap our statistical calculations within each cluster. We first sample 500 sets of 1 000 randomly-chosen measurements from each cluster, allowing replacement of the same value. We then compute our statistics independently for each set, recording the median value of this 1 000-point distribution. This median is used as our overall statistical estimate for the cluster properties. This allows us to compute comparable statistics for each cluster which are not massively biased by their different populations. To test sensitivity, these numerical values (i.e. 500 and 1 000) were varied systematically across an order of magnitude in each direction, with only small changes in the final results.

3.3.3 Final Mapping

Finally, we bin the statistics onto a $0.5° \times 0.5°$ grid to facilitate mapping. For each gridbox, we use the statistics assigned to the geographically-closest cluster centre. If the nearest cluster centre is >300 km away, then we leave the gridbox blank.

Figure 4a and 4b) show maps of the cluster-areas generated for DJF using data from all heights. We see a dense patchwork over the North Atlantic and Western Europe, with larger clusters in other regions. This is representative of the original data distribution (Figure 2). Figure 4c compares the area assigned to each cluster with the midlatitude area of a regular gridbox (dashed lines); most clusters represent an area equivalent to a 2° degree grid or smaller, with almost all representing an area less than than a 5° degree grid.

3.4 Tropopause Calculation

For context, we calculate the tropopause pressure level using daily ERA5 reanalysis output(Hersbach et al., 2020), at full vertical resolution but downsampled to a spatial resolution of $1.5° \times 1.5°$. For each gridpoint, we find the lowest altitude where (a) the vertical temperature lapse rate is $<2\,\mathrm{Kkm^{-1}}$ and (b) this remains true for at least 2 km above this point. We require the tropopause to lie between 700 hPa – 10 hPa, linearly interpolating to find the transition below $2\,\mathrm{Kkm^{-1}}$ as accurately as possible between model levels. Any gridpoints where these criteria are not met are bilinearly interpolated from surrounding gridpoints.

4 Cluster-Generated Maps

Figure 5 shows seasonal maps of median temperatures, zonal winds, and meridional winds between 200 hPa–250 hPa, and the number of measurements assigned to each cluster. Figure 6 shows differences between these data and the ERA5 reanalysis over the same pressure range and period. At this altitude and over this large a height range and time

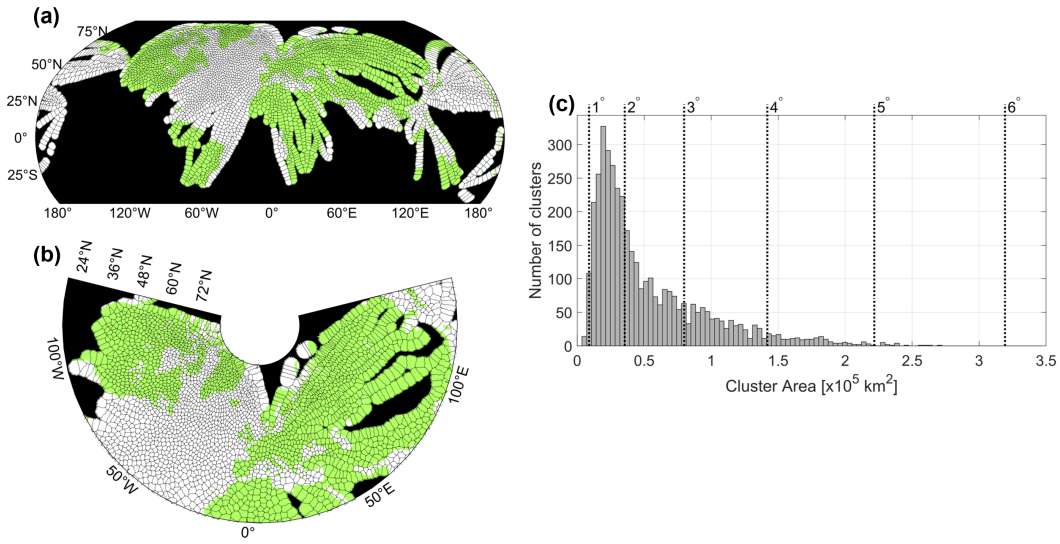

Figure 4. (a,b) Example maps of areas assigned to clusters for (a) all locations with data (b) densely-measured regions of a section of the northern hemisphere. Thin black lines mark perimeters of areas assigned to each cluster; solid black shading indicates no coverage. (c) Histogram showing geographic area assigned to each cluster. Dashed vertical lines indicate the area which would be covered by each cell of a regular latitude-longitude grid (at 45° latitude), indicating that the majority of our clusters represent areas smaller than the average area of a $2^\circ \times 2^\circ$ regular grid. These examples are specifically for the cluster maps generated using data from all heights for the DJF composite season, but broadly resemble those generated for other heights and periods.

period, we expect the reanalysis fields to reasonably approximate true values, and therefore allow us to identify systematic biases created by our sampling pattern. Figure 7 shows GW amplitudes (top rows), G (middle rows) and along-track GW wavelengths (bottom rows) over the same pressure range. We focus on the region 20°N–85°N, 130°W–140°E, due to good sampling in this region.

The maps (except Figure 5y-B) have been smoothed using a 2D Gaussian of FWHM 2.5°×2.5° to facilitate analysis of large scale features. In the unsmoothed data, not shown, small-area orographic wave sources can be clearly identified, especially in the smaller clusters over Europe and the North Atlantic, and these will be studied in more detail in future work.

4.1 Temperature, Wind and Measurement Density

4.1.1 Absolute Value Maps

Figure 5 shows directly-measured variables. These data have been processed identically to the GW data discussed below, to help understand sampling biases.

Temperatures (Figures 5a-d) are low in DJF and high in JJA with a negative meridional gradient from tropics to pole. Standard deviations (Figures 5e-h) are ∼4% or less, with higher internal variability in DJF/MAM and lower internal variability in SON/JJA.

Zonal winds, Figures 5i-l, are strongly positive over the western Atlantic all year and over northern Africa/southern Asia for most of the year, with weaker winds in JJA and stronger in DJF. Winds are moderately strong across most of western North America, especially compared to Eurasia poleward of ∼40°N. Standard deviations (Figures 5m-p) are high over the North Atlantic, consistent with subseasonal variability in jet location. Additional standard deviation peaks are seen east of Asia in MAM, over central Asia in JJA, and over the central USA in DJF and SON; all of these regions also exhibit high absolute values.

Meridional winds (Figures 5q-t) are smaller than zonal, consistent with Figure 3c. Except for JJA, they are negative over western North American, Siberia, the edges of Scandinavia and China, and positive over the North Atlantic, the eastern coast of Russia, and to a lesser degree the Middle East and Iran. JJA exhibits a different morphology, with weaker and less spatially consistent winds over the North Atlantic, positive winds over the Eastern Mediterranean, and positive winds over Siberia. Standard deviations (Figures 5u-x) are largest over the North Atlantic and (again, except JJA) North America.

Measurement density (Figures 5y-B) is greatest on direct great-circle flight paths between Europe and major extra-European population centres, particularly in North America. There is a slight reduction over mainland Europe relative to surrounding locations due to our removal of edge-truncated waves in this region.

4.1.2 Biases Relative to Reanalysis

Figure 6 shows differences from gridded ERA5 output, averaged over the 200–250 hPa range. In general, pointwise differences between IAGOS and reanalysis temperatures and winds should be small (e.g Berkes et al., 2017), and therefore we assume differences represent sampling biases rather than measurement inaccuracies, primarily arising due to aircraft routing optimisations.

Regional temperature differences (Figure 6a-d) are 5 K or less, except for a lightly-sampled region at high latitudes in MAM. Temperatures have a consistent positive bias, except for the far east of Asia and high latitudes near Greenland. Meridional wind differences (Figure 6i-l) are generally patchy, with a positive bias over the North Atlantic

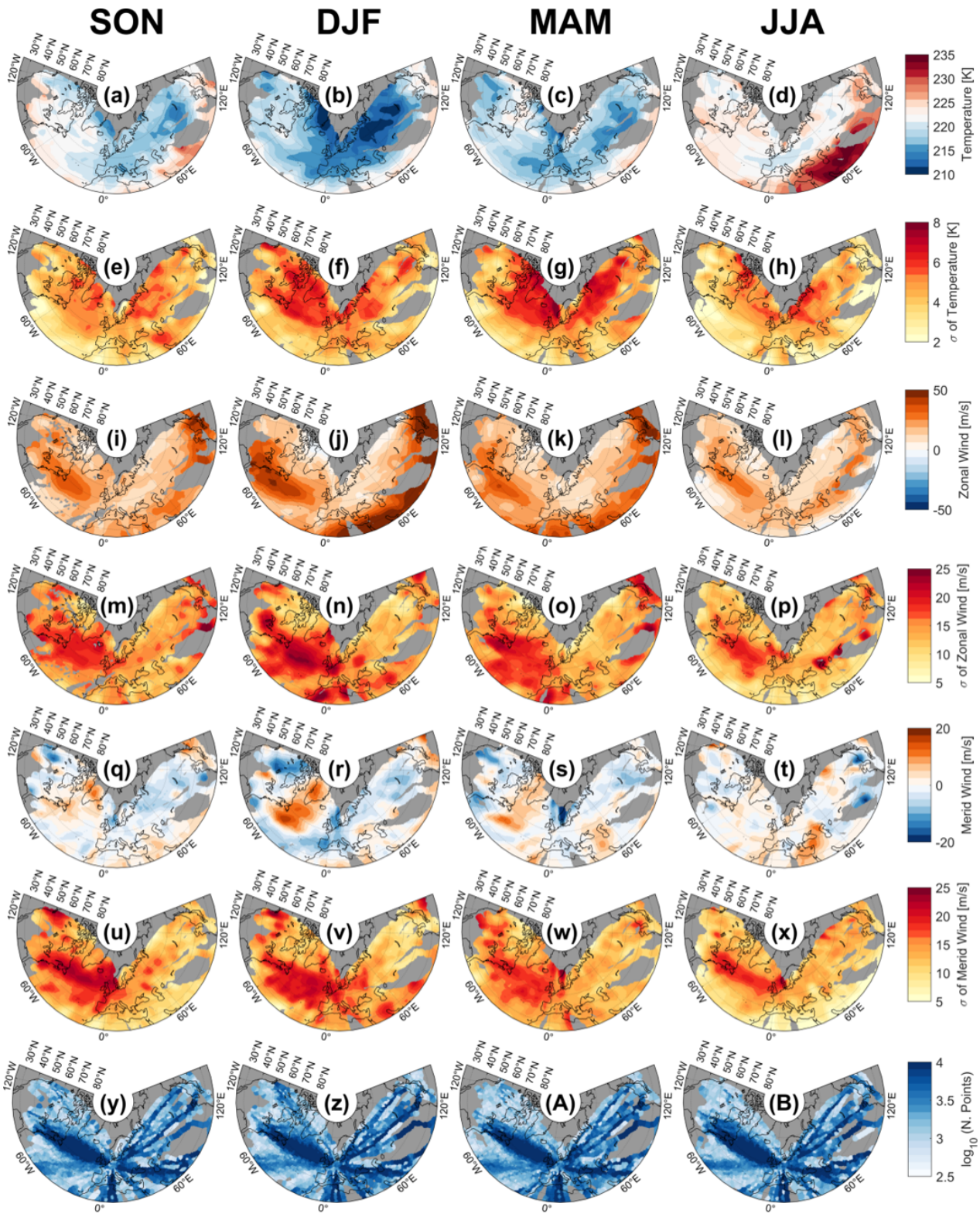

Figure 5. Cluster-analysis derived maps of IAGOS-measured (a-d) temperature, (e-h) standard deviation of temperature, (i-l) zonal wind speed, (m-p) standard deviation of zonal wind speed, (q-t) meridional wind speed, (u-x) standard deviation of meridional wind speed and (y-B) number of measurements, computed over the pressure range 150 hPa – 350 hPa. Figure combines data from all years of IAGOS data. Solid grey shading indicates insufficient data density for analysis, according to the criteria outlined in Section 3.3

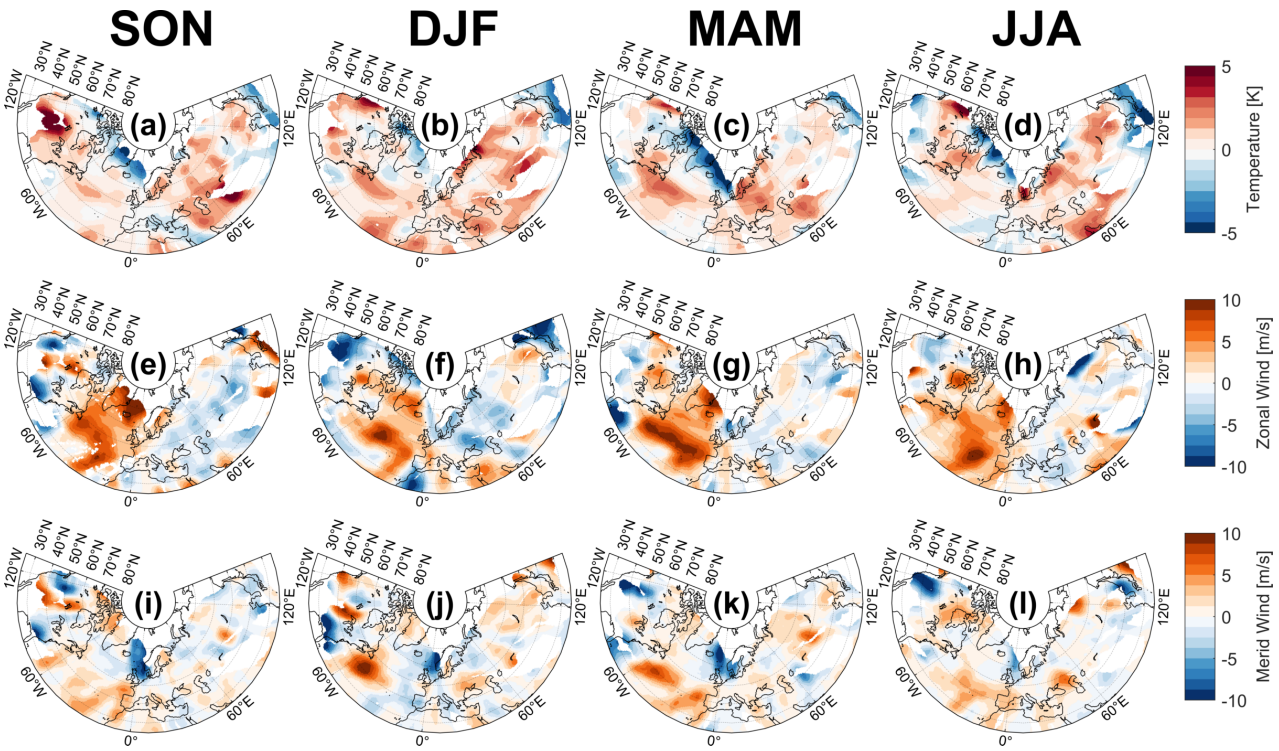

Figure 6. Difference between ERA5 reanalysis and our measured (a-d) temperature, (e-h) zonal wind speed and (i-l) meridional wind speed. Data are computed over the pressure range 150 hPa – 350 hPa for the period August 1994 to December 2019, and are plotted such that a positive value indicates a positive bias in IAGOS relative to ERA5.

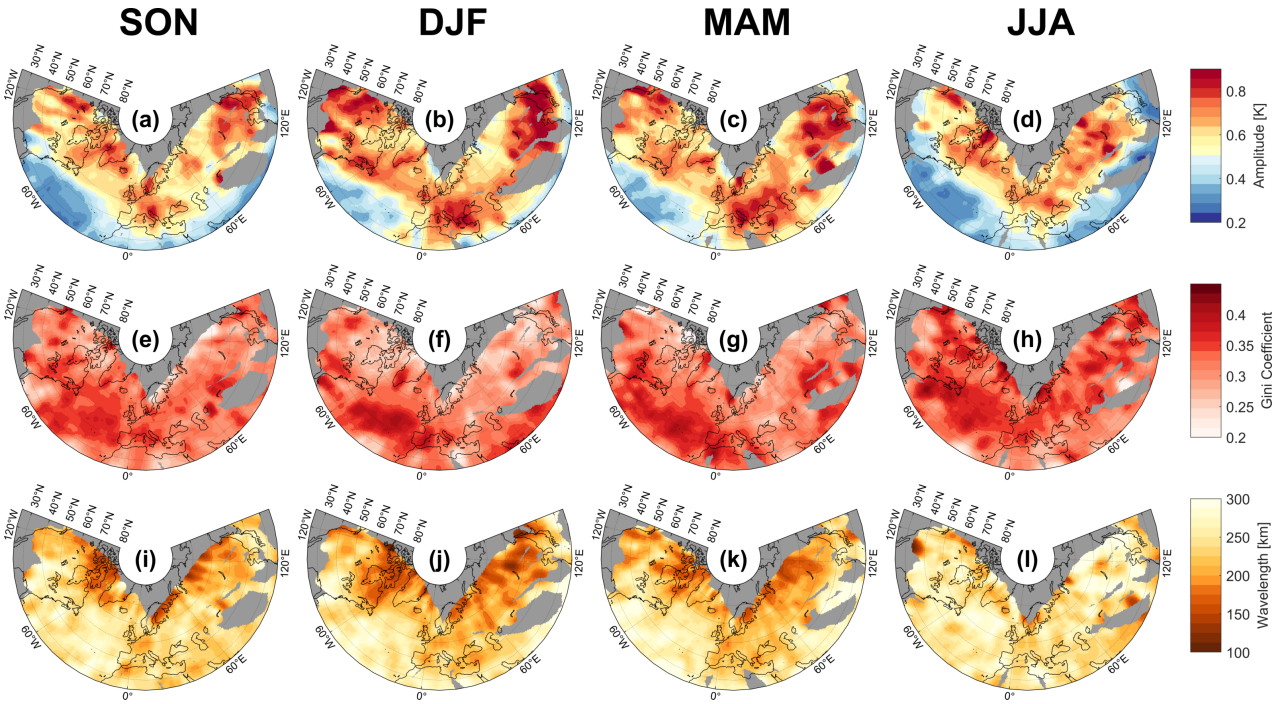

Figure 7. Cluster-analysis derived maps of IAGOS-measured mean GW (a-d) amplitudes (e-h) G and (i-l) along-track wavelengths for (a,e,i) SON (b,f,j) DJF (c,g,k) MAM (d,h,l) JJA, for all data. Figure combines data from all years of IAGOS data.

jet and the central-eastern Atlantic off Africa coast, and a negative bias over Scandinavia and the North Sea. Zonal winds (Figure 6e-h) are the most different field, with patchy biases in most places but with a persistent and large positive bias in the North Atlantic jet stream. This bias is consistent with aircraft flying in the peak of the jet travelling eastwards and avoiding the jet going westwards, leading to a net positive bias when averaged.

4.2 Gravity Waves

GW parameters are shown in Figure 7. Amplitudes (Figures 7a-d) are generally largest in DJF and MAM, and lower in SON and JJA, but with numerous exceptions. They are consistently low over the mid-Atlantic, and consistently high over the North Atlantic and most land poleward of $\sim$40°N. These regions represent a mix of possible wave sources.

Local maxima over southeastern Greenland, western Mongolia, the Sikhote-Alin mountains of Eastern Russia, and the Rocky Mountains of North America are located close to meridionally-aligned ridges, which would be expected to generate wave activity when exposed to strong near-zonal surface winds (e.g. Bacmeister, 1993). G is generally higher than the surrounding area at these locations (except Sikhote-Alin) - this is consistent with orographic wave sources, which tend to be intermittent in nature (Wright et al., 2013).

Many of these orographic signatures are not routinely observed in lower-stratospheric satellite data (e.g Geller et al., 2013). This may suggest that wave momentum generated here is deposited specifically in the lowermost stratosphere. We further discuss the specific case of the Rockies in Section 9.

The strongest clearly non-orographic feature in DJF and MAM is a band of high GW amplitude stretching east from Newfoundland. This band closely mirrors the North Atlantic winter storm track, and is well-resolved due to the high flight density over this region. Measured amplitudes in this band are likely to be skewed slightly high, due to the routing bias discussed above. This makes sense in the context of the dataset: if GWs have the largest amplitudes near the jet, and flights benefit in fuel and travel time from flying nearby on eastward flight legs, then this will skew the measured value anywhere the jet is present during our dataset high relative to other locations. This bias does not imply that there is not a maximum in this band, but merely that we overestimate its relative magnitude. As such, this bias likely enhances the apparent importance of this non-orographic peak with respect to fixed-location orographic hotspots such as southeast Greenland.

G (Figures 7e-h) is generally highest around the Atlantic jet, consistent with the varying jet location. There is also higher G over some orographic regions in winter, consistent with orographic source intermittency, and over large fractions of the observed area in general in JJA.

Wavelengths (Figures 7i-l) are relatively short near the pole in all seasons. We believe this to be a bias arising from the sampling direction of the aircraft trajectories. Aside from this, some regional features can perhaps be seen, with short wavelengths over mountain ranges in DJF and MAM, and (to a minor degree) in patches over the Atlantic Ocean corresponding to regions of high G. In general however, the known difficulties of accurately sampling GW wavelengths from randomly-oriented 1D or 2D cuts through the atmosphere (e.g. Ern et al., 2004) make interpretation of these maps challenging.

We see no evidence of the strong subtropical GW maxima over the Carribean, Africa and South-East Asia usually observed in stratospheric GW observations in JJA (e.g Geller et al., 2013). We believe that, rather than these maxima not being present in the real

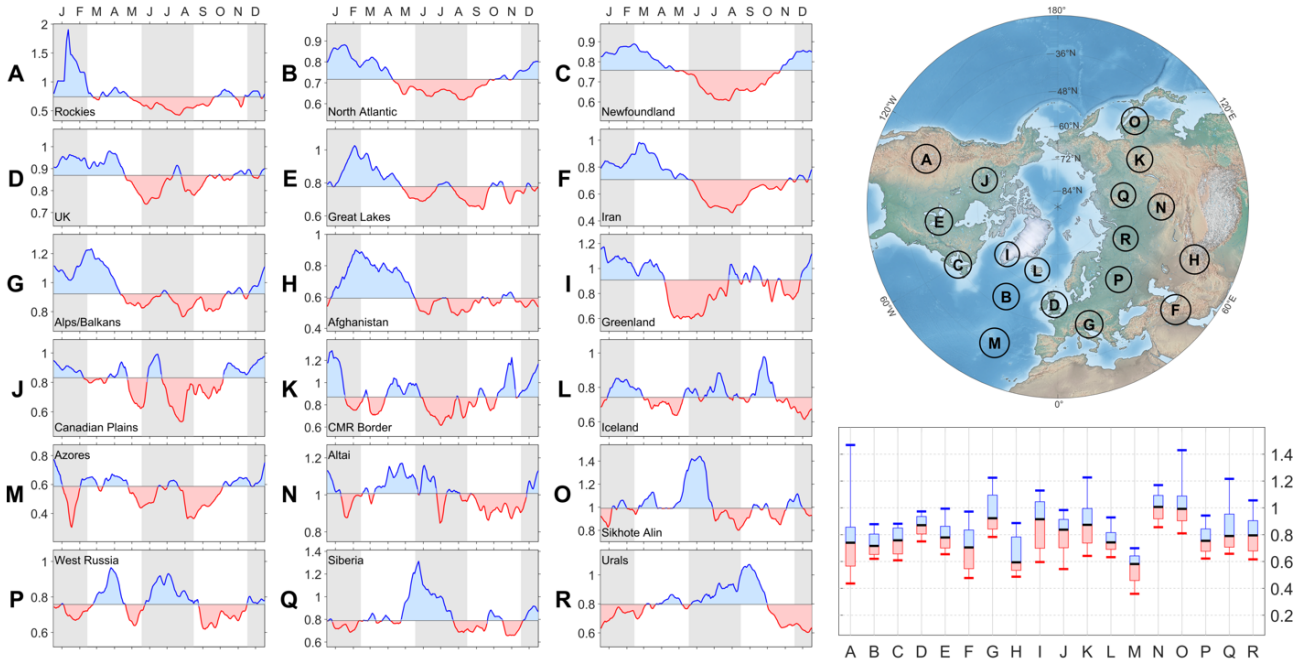

Figure 8. (top right) Map indicating sample regions selected as described in the text. Black circles surrounding each identifying letter show the area averaged. (A-R) Individual composite-year time series at each lettered location. Blue indicates above-median GW amplitudes, red below. Ordinates show wave amplitudes in Kelvin; data have been averaged over a rolling 31-day window. Grey shading indicates the seasons plotted in Figure 7. 'CMR Border' indicates the region at the junction of China, Mongolia and Russia, between the Yablonovy (Russia) and Dà Xīng'ān Lǐng (China) mountain ranges. (bottom right) Box-and-whisker plots showing range of GW amplitudes measured in each region. Upper and lower horizontal lines show the 2.5th and 97.5th percentiles of the data, shaded boxes cover the region between the 18th and 82nd percentiles, and the black solid line indicates the median.

atmosphere, this absence instead is due to aircraft routing biases. Specifically, if these maxima are to a significant extent driven by large-scale storm activity, as seems likely from theoretical, model and satellite evidence, then planes will be routed around rather than through such activity. This will lead to a sharp reduction in relative magnitude in our dataset. However, our available flight metadata do not provide sufficient information to test this hypothesis. The low amplitudes measured over the mid-Atlantic may also be related to such routing choices.

5 Regional Time Series

Figure 8 shows time series of GW amplitude for 18 selected regions, mapped at top right. Most of these regions have been selected visually from Figure 7a-d as local maxima in at least one season, with J, M and P added to fill remaining large spatial gaps in regions of good data coverage.

For each region, median GW amplitude is computed over a rolling 31-calendar-day window, composited over all years and over a geographic circle of radius 500 km indicated by the black circles surrounding the letters. This is done using the original flight-track data, rather than the cluster-analysis output.

Within each region, values above the annual median are shown in blue and below in red. The order of display (i.e. A-R) is selected to to emphasise systematic changes in seasonality: specifically, they are ordered by linear correlation with the Rocky Mountains (region A), selected as (a) arbitrarily, it is the westernmost region and (b) subjectively, it has a clear seasonal cycle. Time series most similar to A are assigned earlier letters alphabetically. Sequences of alphabetically-close letters on the map therefore indicate consistent GW-amplitude seasonality at supraregional geographical scales.

At bottom right, the spread of amplitudes in panels A-R is illustrated, allowing comparison between the scaled time series. For each region, a box-and-whisker plot is shown, highlighting the range between the 18th and 82nd percentiles (box, equivalent to the first standard deviation of a normal distribution) and between the 2.5th and 97.5th percentiles (whiskers, equivalent to the the two standard deviation range).

Regions A-H show clear seasonal cycles with maxima in winter/early spring, and minima in summer/early autumn. Regions I-P then show multiple minima and maxima, while regions Q and R are largely in antiphase with A-H and peak in summer.

Spatial groupings with strong similarities in seasonal cycle and median amplitude can be seen in the data. These include a broad curve sweeping from the Rocky Mountains across the Atlantic to central Europe (A-E,G), a Central Asian grouping (N-Q), and pairs in Greenland/Iceland (I, L) and the Middle East (F,H). These groups are distributed in zonal bands, with relatively short meridional distances leading to much larger differences in seasonal cycle. For example, regions I,J,L and M lie spatially close to individual members of the A-E, G grouping, but exhibit large differences from this group. These strong meridional gradients are consistent with the seasonal-level view seen in Figure 7, but are shown here to be applicable at the subseasonal level.

6 The Effect of the Upper Tropospheric Jet on Observed Gravity Waves

In Section 4 we saw a clear pattern over the North Atlantic of large GW amplitudes to the north of the wind jets. In this Section, we investigate this feature in more depth by examining the height dependence of GW amplitude and wind in the zonal mean.

Figures 9a-d show zonal-mean GW amplitudes, binned onto a grid of height 5 hPa and width 4° latitude. Mean tropopause pressure is indicated for context (thick black lines). This has been weighted spatially and temporally in the same way as the observations, although importantly that there is significant variability in this level. Figures 9e-h show zonal mean zonal winds derived in the same way, while Figures 9j-m show the zonal sum of individual measurements, peaking at around three million ($10^{6.5}$) data points per gridbox.

These figures have been adjusted for the uneven longitude distribution of the data by first gridding onto a 30° grid in longitude and then taking the zonal mean (or sum, for Figures 9j-m). However, some bias is unavoidable, and in particular the Pacific Ocean and the southern hemisphere away from routes between Europe and a small number of major airports are significantly underrepresented. Due to highly limited data coverage south of the Equator, we restrict the following discussion to the northern hemisphere; however, we note that based on the limited data available, it appears likely that most of our northern hemisphere conclusions are mirrored at least as far as ∼40°S.

We consider first zonal mean zonal winds, Figures 9e-h. We see a clear jet spanning all measured heights in all four seasons, centred at ∼25°N in DJF and ∼40°N in JJA. The jet is strongest in DJF and weaker in JJA, consistent with the expected climatological state of the UTLS, and in general increases in speed with height across our data range.

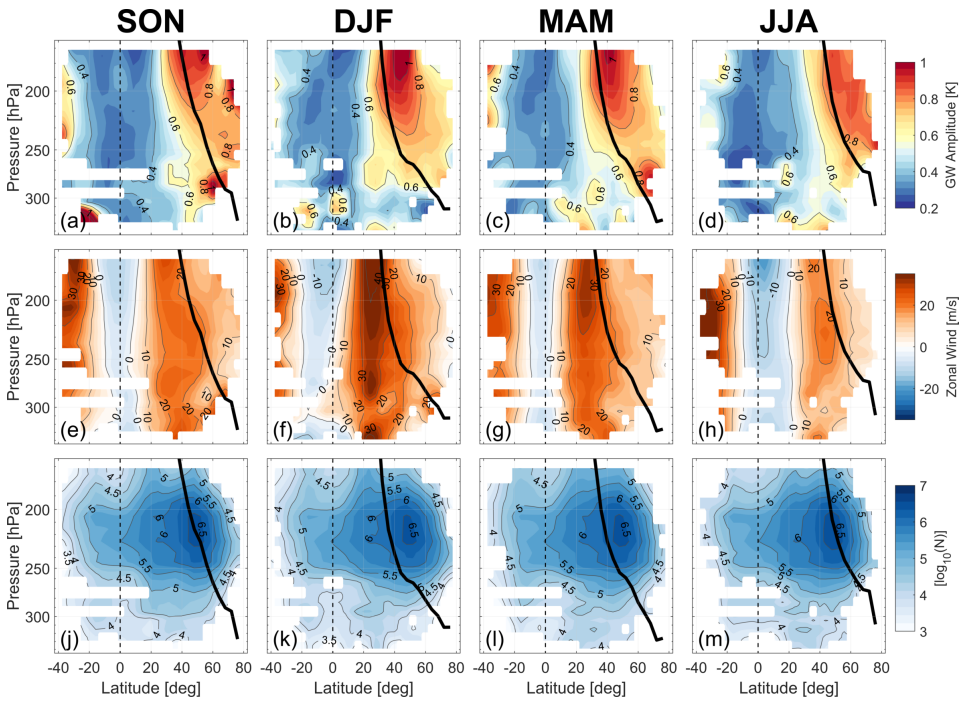

Figure 9. Seasonal plots of IAGOS-derived (a-d) zonal mean GW amplitude (e-h) zonal mean zonal wind (j-m) zonal-sum number of measurements for (a,e,j) DJF (b,f,k) MAM (c,g,l) JJA (d,h,m) SON, as a function of (vertical axis) pressure level and (horizontal axis) latitude. Thick black line indicates mean tropospheric pressure level, derived from ERA5 data computed at IAGOS measurements locations.

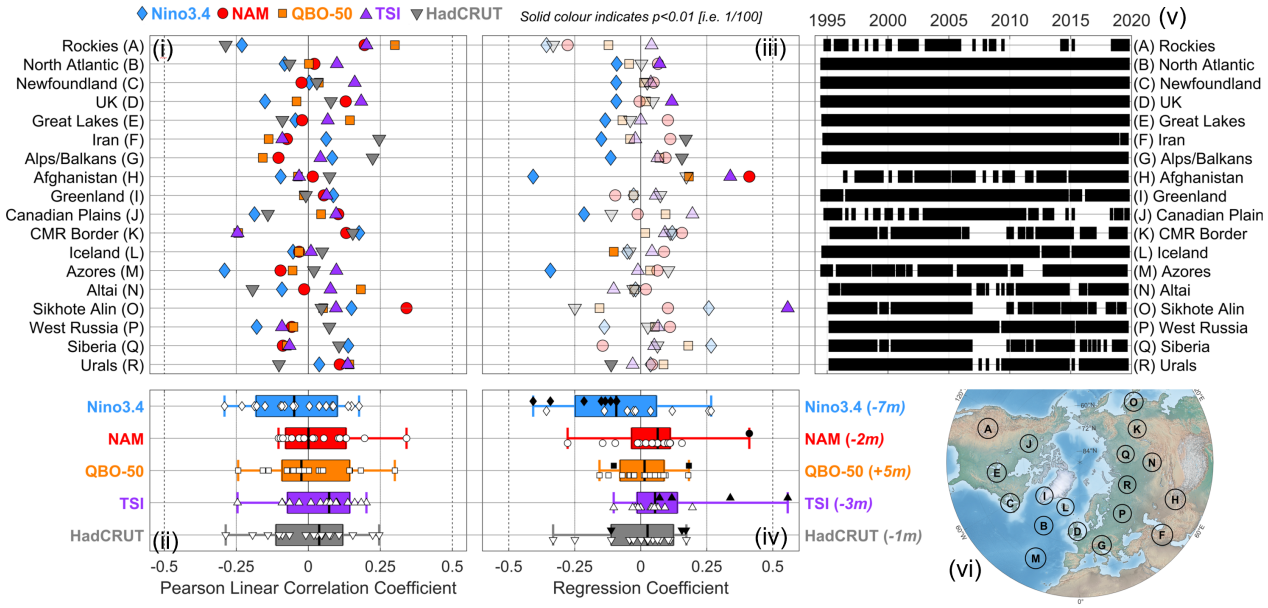

Figure 10. Analyses of possible gravity wave driving mechanisms. (i,ii) Pearson linear correlation coefficient between GW amplitudes for each region defined in Figure 8 and the El Nino 3.4 index (Nino3.4), Northern Annular Mode index (NAM), 50 hPa QBO zonal winds (QBO-50), Total Solar Irradiance (TSI), and the Hadley Central/ Climate Research Unit surface temperature index (HadCRUT). (i) shows each region individually, (ii) shows statistics for all regions combined. Box-and-whisker plots are as described in Figure 8; individual white symbols correspond to the points in panel (i). (iii) Results of a linear regression applied to each region based on the described indices, at a lag described by the y-axis of panel (iv) for each dataset in months. Solid (semi-transparent) symbols show significant (non-significant) results at the p=0.01 level. (iv) As (iii), for all regions combined. White (black) markers indicate (non-) significant results. (v) Temporal coverage for each region, at the monthly scale. Solid black indicates data coverage over the region that month. (vi) Region map, reproduced from Figure 8.

We next examine zonal mean GW amplitudes, Figures 9a-d. Larger GW amplitudes are clearly visible in the stratosphere, i.e. above the thick black line, and these amplitudes generally increase with height (with minor exceptions). Maximal GW amplitudes at each latitude are seen slightly poleward of and above the jet in all four seasons. Amplitudes are generally lower in the troposphere and higher in the stratosphere, and outside the tropics they in general grow with altitude, with the exception of some small patches at high latitudes in DJF and a disconnect between a low-altitude near-pole region and a higher-altitude midlatitude peak in MAM. There is also evidence of lower-altitude maxima at around 40°N and 300 hPa in DJF and MAM, which lie within the jet but are disconnected from the larger regions of high amplitude in the stratosphere.

7 Climate Drivers of Gravity Wave Variability

A unique benefit of these data is the combination of long duration and wide spatial coverage. Long-term records capable of resolving gravity wave activity over such large spatial regions are rare, and we believe this to be the largest and longest such dataset. As such, our data provide a unique opportunity to assess the role of long-term climate processes in driving or modulating GW activity.

In Figure 10 we compare GW amplitude time series from the 18 regions defined in Figure 8 to five climate indices - 'Nino3.4', representing the El-Nino Southern Oscillation (ENSO), 'NAM', representing the Northern Annular Mode, 'QBO-50', representing Quasi Biennial Oscillation-driven equatorial wind speeds at 50 hPa, 'TSI', representing the time-varying output of the Sun, and 'HadCRUT', representing long-term changes in surface temperature (Trenberth & Stepaniak, 2001; Ogi et al., 2004; Morice et al., 2012; Coddington et al., 2015). Our HadCRUT4 time series is computed over the Northern Hemisphere only, since all regions lie here and relationships in the southern hemisphere may differ due to the very different relationship between GWs and the southern polar vortex.

We first bin our data onto a monthly timescale over the 26 years of data, averaging in all cases over the 500 km radius areas shown in Figure 8 and reproduced in Figure 10vi for context. Figure 10v (top right) shows the temporal coverage available after this binning - most regions are well-covered over the full duration of the dataset, with the possible exception of the Rocky Mountains (region A).

Figures 10i-iv then compare our GW amplitude time series to the five climate indices, using Pearson linear correlation (Figures 10i-ii) and multiple linear regression (Figures 10iii-iv). All time series, both GW and index, have been boxcar-smoothed by three months, except for the rapidly-varying NAM and GW series which we compare to it.

7.1 Correlations

We first discuss linear correlations, Figure 10i-ii. Figure 10i shows correlations between each index and GW amplitudes within individual regions. Coloured markers, described by the key at top, show linear correlation between GW amplitudes and each climate index in the region. 10ii compresses these correlations into a single box-and-whisker plot for each index, with individual regions overlaid with markers.

We see extreme scatter, with little consistency between the results and significant inter-region variability for correlations with every metric. Except for the relatively-poorly-measured Rocky Mountains (A) and one other point (the NAM and the Sikhote Alin, Region O) we see no correlations exceeding an absolute value of 0.25. There is perhaps a very slight positive skew to the set of correlations between GW amplitudes and TSI, but this is weak and nearly a quarter (5/24) of these correlations are negative. Daily data were also examined, with broadly similar results; these daily data were also lagged over the range -70 to +70 days, but no lag value was found to systematically improve the correlation with any index over a majority of regions.

7.2 Linear Regression

Figures 10iii-iv show the results of a multiple linear regression applied to the same combinations of GW measurements and indices. As with the correlations, the upper panel shows results for individual regions and the lower panel combined results.

To compute comparable regression coefficients, we normalise each index. For all except HadCRUT, we convert to relative ranges, i.e. a mean of zero and range of one over the period August 1994 to December 2019. For HadCRUT, which is non-cyclical, this conversion is less meaningful, and we keep the original units of Kelvin. This produces similar numerical values to the other comparisons since the full range is of order 1 K. Thus, for all indices except HadCRUT, a coefficient of +1 suggests that a change from the minimum index value over this period to the maximum leads to a 1 K increase in monthly-mean gravity wave amplitude, while for HadCRUT it implies that a 1 K increase in global-mean surface temperature leads to the same change.

We repeat the regression at time lags from -11 months to +11 months, then sum the absolute regression coefficient for each index and maximise to identify the lag which provides the best estimated fit for that index across all regions. This best fit lag is the one displayed in our Figure, and the lag period in months is indicated in the y-axis labels on Figures 10iv, with a positive value indicating that the gravity wave signal leads the index and vice-versa.

We encode the p-value of the t-statistic for each fit using colour density in the upper panel. Solid-coloured markers are significant at the $p<0.01$ level, while semi-transparent markers (the vast majority) are not. In the lower panel this information is encoded with marker colour, where black markers are significant at the 0.01 level. A threshold of 0.01 is chosen due to the nature of the comparison. A typical threshold of 0.05 would imply that the null hypothesis was false in 1/20 cases just by chance; since we here make 90 (5x18) comparisons we would therefore expect 5 of these to be marked as significant regardless of the actual truth. By using a much lower threshold, we reduce this random effect. This test assumes independence of the measured amplitude series, which is an inherently poor assumption for geophysical data and becomes increasingly less likely to be the case as locations become spatially closer; therefore, these values must be considered sceptically.

This choice to use a single lag for each index over all regions is made to simplify the presented results, and it may well be the case that some regions have significant and physically meaningful effects at different lags to others; this may therefore be a fruitful pathway for future work.

The most interesting results are for ENSO, shown as blue diamonds. In nine of our eighteen regions we see a statistically-significant link, with an increase in ENSO associated with a drop in GW amplitudes seven months earlier. This reduction is of 0.15–0.4 K/cycle, i.e. a maximal El Niño leads to GW amplitudes 25-60% higher than a minimum La Niña, with a seven-month teleconnective lag. All regions which do not exhibit this lag-relationship, excluding the poorly temporally sampled Rockies, are not identified as statistically significant and also fall within two distinct geographic groups: Greenland/Iceland and Russia (recall from Figure 8 that most Russian regions also have a very different seasonal cycle to the majority of our data). These data therefore represent evidence of strong teleconnective links between the Pacific Ocean and gravity wave generation, propagation and/or filterig in the troposphere and UTLS over North America, Europe, South-Central Asia and the non-Arctic Atlantic Ocean.

Other indices produce less clear results, but still present some interesting conclusions, although not as strong as for ENSO. Aside from ENSO, we see ten statistically-significant linkages - this is higher than would be expected by chance assuming independence, but since the atmospheric system is inherently highly linked needs to be treated with scepticism.

For the NAM, only one region shows a significant relationship, Afghanistan (H), at a lag of two months. This region is spatially distant from the NAM foci in the North Atlantic, Arctic and Pacific, and a physical mechanism which could link the NAM to this region and no surrounding ones is not immediately obvious. Therefore, we are disinclined to believe this is a meaningful or real teleconnection.

The QBO shows two significant results, but these are in antiphase with each other and spatially disparate. All other results are scattered across regression coefficient space, mostly at relatively small values, and it is thus difficult to conclude that these are truly meaningful signals. Similarly, three regions show a significant relationship with HadCRUT, but again with both positive and negative significant points and with a range of regional values, most clustered near zero.

TSI is slightly more interesting. At a lag of three months, there are four significant points, all positive in sign. 10 of the 14 non-significant points are also positive, as are most correlations presented in Figure 10ii. Finally, a three-month lag is a physically reasonable time for a teleconnective signal such as this to operate, and since solar input is global a mechanistic pathway to a particular region is not needed, as with the NAM. Therefore, although we have insufficient data to draw any firm conclusions, our results may present weak evidence of a positive link between the solar cycle and NH UTLS GWs, with solar maximum corresponding to increased GW amplitudes.

8 Validation

The height range, spatiotemporal coverage and in-situ nature of our dataset is unusual, and also has several inherent systematic biases. Therefore, it is important to validate our results against other long-term UTLS GW time series.

8.1 United States Radiosondes

Wang and Geller (2003) (WG03) examined GW energy densities derived from high-resolution radiosondes over the United States for the period 1998–2001 in two height bands - a tropospheric (2–8.9 km) band below and a stratospheric (∼18–24.9 km) band above our analysis (∼10–12 km altitude). In their tropospheric band (their Figure 5), WG03 saw strong GW activity over the Rockies and western USA throughout the year, over the northwestern US in DJF, and low activity otherwise. In the stratospheric band (their Figure 6), they saw only weak GW activity over the Rockies (except for a slight enhancement over Wyoming in DJF), but significant activity in the southern and eastern US in DJF, in the south only in MAM, and over Oklahoma in SON.

Our maps (Figure 7) share many features with these results. In DJF, we see good agreement, with strong GW activity over the US Rockies and as much as our data cover of the eastern seaboard and southeastern US, consistent with a mixture of the two layers of WG03. In MAM, we see GW activity in the western US consistent with their tropospheric band, but do not see major activity over the southern US (although our data are truncated near this region, and data density is often poor in the areas our data do cover). In JJA/SON our results are less consistent with WG03, with good agreement in most places but lacking their strong signal over the Rockies.

8.2 North Atlantic Radiosondes

Plougonven et al. (2003) describe GW measurements from 224 radiosondes launched from ships in the North Atlantic (30–70°N, 50–0°W) during the FASTEX campaign in January/February 1997. They focused on short vertical wavelength features (<5 km), which they studied in the context of the jet up to 20 km. They saw GW activity centred on the jet axis in both the stratosphere and troposphere, peaking on the north side in the stratosphere, with a nominal maximum 300 km from jet centre but with extremely large scatter (their Figures 2 and 5). Our peak GW activity is consistently to the north side of the jet but slightly further away, with a maximum between 5° and 10° north of the jet core. However, given the very high degree of scatter in the data of Plougonven et al. (2003), these conclusions are not inconsistent.

8.3 Greenland Aircraft Turbulence Encounters

Lane et al. (2009) describe statistics of aircraft turbulence encounters over Greenland, derived from aircraft instrument reports. These events primarily arise due to interactions between GWs emitted from Greenland's orography and background directional wind shear. They see a near-annual cycle in these reports, with peaks in November and

January and a trough in May. The winter peaks and May trough are consistent with our data (Figure 8I), but we also see a secondary maximum in August/September which they do not.

8.4 Aberystwyth MST Radar

Vaughan and Worthington (2007) studied inertia-GWs using eight years of data from the MST Radar in Aberystwyth, Wales (within our region D). They observed a winter peak in occurrence rate. While these results carry the important caveat that they explicitly aimed to exclude the orographic waves that likely form a significant proportion of our data in this region, their results were again consistent with ours.

8.5 European Satellite Cloud Imagery

Cruette (1976) studied lee waves patterns in satellite cloud imagery from the mid-troposphere in western Europe over three years of data. She saw a strong seasonal pattern over an area including the UK (region D) and western Alps (edge of our region G), with a peak in winter and trough in summer, again consistent with our results.

8.6 CHAMP Estimates of Russian Lower-Stratospheric GW Seasonality

Independent estimates of UTLS GW seasonality over Russia and Central Asia (regions N-R) have proven challenging to locate in the literature. This is a major issue, because the observed GW seasonality in our data in these regions is opposite to most other regions and to a more general assumption that GW amplitudes will be on average higher in winter due to the nature of most source mechanisms.

Some very limited evidence to support the observed seasonality is seen in Namboothiri et al. (2008), where CHAMP-derived GW variances at 20 km altitude for 2002 exhibit larger values in JJA than DJF by a factor of 4, but from a low base. However, this evidence is from an experimental instrument type over only a short duration, and longer-term measurements at 30 km altitude from the more modern HIRDLS and SABER instruments (Ern et al., 2018) do not show this, peaking instead in January.

We note clearly that the observed seasonality could be correct. A plausible mechanism, for example, would be non-orographic generation from summer storms which, deep in the continent, will not be modulated strongly by the North Atlantic jet stream. The annual cycle of rainfall in this region is consistent with this mechanism, and filtering, horizontal propagation, or observational filter differences could easily explain the lack of observed signal at 30 km. However, given the lack of validation, it is important to remain sceptical of these specific results until further evidence is available.

9 Implications of Strong GW Activity over the Rockies

In our data (e.g. Figure 7), we see large amplitudes over the Rocky Mountains (region A). However, similar activity is not usually observed in stratospheric satellite data, including measurements at altitudes as low as 20 km altitude (∼50 hPa) made using HIRDLS/Aura (e.g. Geller et al., 2013; Wright et al., 2015; Ern et al., 2018). While poorly temporally sampled in the early 2010s (Figure 10), the total number of measurements over this region in earlier years is sufficient to properly characterise the seasonal cycle (Figures 5y-B), and thus discussion of this mismatch is a meaningful question.

The specific comparison to HIRDLS is important. Over the Rockies, IAGOS aircraft usually travel near-meridionally, as long-haul flights to Europe dominate the dataset. As such, their along-track vector is very similar to Aura, which has a polar orbit at 98°

inclination. Alternate HIRDLS profile-pairs are spaced ∼40 km apart at 20 km altitude (e.g. Figure 4b of Wright et al., 2015), and thus there should be some degree of observational filter overlap between the shortest waves visible to HIRDLS and longer waves seen by IAGOS, which have mean wavelengths in this region of ∼150-250 km with a standard deviation (not shown) of ∼100 km.

However, HIRDLS data show neither enhanced GW activity (e.g. Geller et al., 2013; Wright et al., 2015; Ern et al., 2018) over the Rockies, nor the intermittency characteristic of orographic wave sources in the statosphere (Wright et al., 2013), even when filtered to identify only the shortest accessible lengthscales (Figure 7 of Wright et al., 2015). Assuming the waves seen here are orographic and therefore propagate mostly vertically, which seems likely given their geographic location and relatively large amplitudes, this suggests three possibilities: (a) that the waves break between ∼200 hPa–50 hPa (∼10–20 km altitude), (b) that the waves propagate into the stratosphere, but only have extremely short horizontal wavelengths and are thus invisible to HIRDLS, or (c) that the waves are invisible to HIRDLS due either to their phase fronts being aligned along the instrument boresight (e.g. Figure 1 of Wright & Hindley, 2018) or due to having vertical wavelengths <∼2–3 km.

Option (b) is unlikely as observations with AIRS/Aqua, which measures short-horizontal long-vertical wavelength waves, also show no significant stratospheric wave activity over the Rockies (Hoffmann et al., 2013). This restricts the possible wavelengths of any waves propagating into the stratosphere to small scales in both the vertical and horizontal. Also, our median horizontal wavelength is in the HIRDLS observational filter, so at least some signal would be expected to be visible unless there was a dramatic shift in horizontal wavelength between the two heights.

Option (c) is also unlikely as the HIRDLS boresight, which points at 47° off the orbital track, will be aligned at a high angle to the zonally-aligned waves the relative orientations of the winds and mountain ridge in this region would imply (Bacmeister, 1993), while short vertical wavelengths would preclude sharp vertical ascent.

It is therefore likely that the waves we observe here break in the UTLS, driving the winds specifically in this geographic and height region. This contrasts with many models (Geller et al., 2013), which propagate significant quantities of wave momentum flux into the statosphere over the Rockies.

10 Discussion

The data used have significant, but known, biases and deficiencies. The biggest such deficiency is that the data are one-dimensional, lacking vertical and cross-track spatial information. This prevents us from estimating momentum fluxes and other important GW properties, and complicates interpretation of our results. While we do not do so here, the combination of horizontal wavelength and wind speed can in principle be used to estimate vertical wavelength provided very significant assumptions are made (e.g. M. J. Alexander & Grimsdell, 2013), and this may be useful for future work. The lack of cross-track information is a problem common to stratospheric limb sounding studies of GWs which is harder to adjust for, and therefore we have in general avoided discussion of horizontal wavelengths, except in Section 9 where the relative orientations of the measurements platforms being compared are known.

Biases include flight routing around storms, which may explain the lack of subtropical amplitude maxima in our summer data, a bias towards shorter wavelengths at the start of our routes due to spectral edge truncation, limited spatiotemporal coverage outside major flight paths, and a preference for flights to fly in the jet eastwards and away from the jet westwards leading to a likely positive skew over the North Atlantic in measured wave amplitudes. These biases are discussed in the text where appropriate. With

the exception of the storm routing bias and to a lesser degree the jet-flight bias, these are likely to be systematic across the dataset rather than seasonally-varying, and thus should not significantly affect our time-series analyses for most regions.

11 Summary and Conclusions

We have analysed 26 years of UTLS GW measurements derived from commercial flight data, primarily over the northern hemisphere. This dataset is uniquely long for a large area dataset suitable for GW research, allowing us to study important effects inaccessible with other tools.

We show regionally-varying seasonal cycles, with regional similarities primarily in the zonal direction. Our results include strong GW signals associated with orographic sources which are not seen in stratospheric satellite data. The strongest and most consistent GW amplitudes are seen above and to the north of the upper tropospheric jet, and over orographic hotspots such as south-east Greenland, East Asia and the Rocky Mountains.

Analysis of the relationship between our long-timeseries data and multiple climate-system indices show no significant relationship with the QBO, climate change or the NAM. There may be weak evidence of a link with solar output 3 months earlier, although this is not statistically significant in most regions.

We do however see statistically-significant evidence in all studied regions other than Russia and the Arctic of a seven-month-lagged link with El Niño, with positive-phase ENSO leading to an increase in GW amplitudes in these regions of order 25%. A qualitative relationship between ENSO and UTLS GWs was previously suggested by Wang and Geller (2003) on the basis on four years of United States radiosonde data as a possible explanation for differences between their annual distributions, but here we advance significantly upon this earlier work by (a) demonstrating the link over a much larger area, (b) showing that it is statistically significant, and (c) and quantifying the change it induces in the wave field.

Acknowledgments

We would like to thank Manoj Joshi (UEA) for useful comments at the 2020 UK Climate Dynamics Meeting on possible mid-Eurasian wave sources and inter-region comparisons, Paul Williams (Reading) for useful comments via email on aircraft routing around storms, and Neil Hindley (Bath) for providing the improved S-Transform code and for several useful comments relating to our data analysis pipeline. C.J. Wright is funded by Royal Society University Fellowship UF160545 and by NERC grants NE/R001391/1 and NE/S00985X/1. T.P. Banyard is funded by an EPSRC Doctoral Training Account awarded to the University of Bath and by Royal Society grant RGF/EA/180217. IAGOS data are available from the IAGOS Data Portal. Software produced to generate the data and figures is available from https://github.com/corwin365/2020_IAGOS_GW_Study

References

Alexander, M. J., Geller, M., McLandress, C., Polavarapu, S., Preusse, P., Sassi, F., ... Watanabe, S. (2010). Recent developments in gravity-wave effects in climate models and the global distribution of gravity-wave momentum flux from observations and models. *Quarterly Journal of the Royal Meteorological Society*. doi: 10.1002/qj.637

Alexander, M. J., Gille, J., Cavanaugh, C., Coffey, M., Craig, C., Eden, T., ... Dean, V. (2008). Global estimates of gravity wave momentum flux from High Resolution Dynamics Limb Sounder observations. *Journal of Geophysical*

Research, *113*(D15). doi: 10.1029/2007jd008807

Alexander, M. J., & Grimsdell, A. W. (2013). Seasonal cycle of orographic gravity wave occurrence above small islands in the southern hemisphere: Implications for effects on the general circulation. *Journal of Geophysical Research: Atmospheres*, *118*(20), 11,589-11,599. doi: 10.1002/2013JD020526

Alexander, S. P., Klekociuk, A. R., McDonald, A. J., & Pitts, M. C. (2013). Quantifying the role of orographic gravity waves on polar stratospheric cloud occurrence in the antarctic and the arctic. *Journal of Geophysical Research: Atmospheres*, *118*(20), 11,493-11,507. doi: 10.1002/2013JD020122

Bacmeister, J. T. (1993). Mountain-Wave Drag in the Stratosphere and Mesosphere Inferred from Observed Winds and a Simple Mountain-Wave Parameterization Scheme. *Journal of the Atmospheric Sciences*, *50*(3), 377-399. doi: 10.1175/1520-0469(1993)050⟨0377:MWDITS⟩2.0.CO;2

Berkes, F., Neis, P., Schultz, M. G., Bundke, U., Rohs, S., Smit, H. G. J., ... Petzold, A. (2017). In situ temperature measurements in the upper troposphere and lowermost stratosphere from 2 decades of IAGOS long-term routine observation. *Atmospheric Chemistry and Physics*, *17*(20), 12495–12508. doi: 10.5194/acp-17-12495-2017

Boulanger, D., Thouret, V., & Petzold, A. (2019). *IAGOS Data Portal.* AERIS. Retrieved from `http://www.iagos-data.fr/` doi: 10.25326/20

Callies, J., Bühler, O., & Ferrari, R. (2016). The dynamics of mesoscale winds in the upper troposphere and lower stratosphere. *Journal of the Atmospheric Sciences*, *73*(12), 4853–4872. doi: 10.1175/jas-d-16-0108.1

Callies, J., Ferrari, R., & Bühler, O. (2014). Transition from geostrophic turbulence to inertia–gravity waves in the atmospheric energy spectrum. *Proceedings of the National Academy of Sciences*, *111*(48), 17033–17038. doi: 10.1073/pnas.1410772111

Cho, J. Y. N., & Lindborg, E. (2001). Horizontal velocity structure functions in the upper troposphere and lower stratosphere: 1. observations. *Journal of Geophysical Research: Atmospheres*, *106*(D10), 10223–10232. doi: 10.1029/2000jd900814

Coddington, O., Lean, J. L., Lindholm, D., Pilewskie, P., Snow, M., & NOAA CDR Program. (2015). *NOAA Climate Data Record (CDR) of Total Solar Irradiance (TSI), NRLTSI Version 2.* NOAA National Centers for Environmental Information. Retrieved from `https://data.nodc.noaa.gov/cgi-bin/iso?id=gov.noaa.ncdc:C00828` doi: 10.7289/V55B00C1

Cruette, D. (1976). Experimental study of mountain lee waves by means of satellite photographs and aircraft measurements. *Tellus*, *28*(6), 499–523. doi: 10.3402/tellusa.v28i6.11318

Ern, M., Preusse, P., Alexander, M., & Warner, C. (2004). Absolute values of gravity wave momentum flux derived from satellite data. *Journal of Geophysical Research*, *109*(D20). doi: 10.1029/2004jd004752

Ern, M., Trinh, Q. T., Preusse, P., Gille, J. C., Mlynczak, M. G., III, J. M. R., & Riese, M. (2018). GRACILE: a comprehensive climatology of atmospheric gravity wave parameters based on satellite limb soundings. *Earth System Science Data*, *10*(2), 857–892. doi: 10.5194/essd-10-857-2018

Fritts, D. C., & Alexander, M. (2003). Gravity wave dynamics and effects in the middle atmosphere. *Reviews of Geophysics*, *41*(1). doi: 10.1029/2001rg000106

Geller, M. A., Alexander, M. J., Love, P. T., Bacmeister, J., Ern, M., Hertzog, A., ... Zhou, T. (2013). A comparison between gravity wave momentum fluxes in observations and climate models. *Journal of Climate*, *26*(17), 6383–6405. doi: 10.1175/jcli-d-12-00545.1

Hersbach, H., Bell, B., Berrisford, P., Hirahara, S., Horányi, A., Muñoz-Sabater, J., ... Thépaut, J.-N. (2020). The ERA5 global reanalysis. *Quarterly Journal of*

the Royal Meteorological Society. doi: 10.1002/qj.3803

Hindley, N. P., Wright, C. J., Smith, N. D., Hoffmann, L., Holt, L. A., Alexander, M. J., ... Mitchell, N. J. (2019). Gravity waves in the winter stratosphere over the southern ocean: high-resolution satellite observations and 3-d spectral analysis. *Atmospheric Chemistry and Physics*, *19*(24), 15377–15414. doi: 10.5194/acp-19-15377-2019

Hindley, N. P., Wright, C. J., Smith, N. D., & Mitchell, N. J. (2015). The southern stratospheric gravity wave hot spot: individual waves and their momentum fluxes measured by COSMIC GPS-RO. *Atmospheric Chemistry and Physics*, *15*(14), 7797–7818. doi: 10.5194/acp-15-7797-2015

Hoffmann, L., Xue, X., & Alexander, M. J. (2013). A global view of stratospheric gravity wave hotspots located with Atmospheric Infrared Sounder observations. *Journal of Geophysical Research: Atmospheres*, *118*(2), 416–434. doi: 10.1029/2012jd018658

Kuchar, A., Sacha, P., Eichinger, R., Jacobi, C., Pisoft, P., & Rieder, H. E. (2020). On the intermittency of orographic gravity wave hotspots and its importance for middle atmosphere dynamics. *Weather and Climate Dynamics Discussions*. doi: 10.5194/wcd-2020-21

Lane, T. P., Doyle, J. D., Sharman, R. D., Shapiro, M. A., & Watson, C. D. (2009). Statistics and dynamics of aircraft encounters of turbulence over Greenland. *Monthly Weather Review*, *137*(8), 2687–2702. doi: 10.1175/2009mwr2878.1

Li, Q., & Lindborg, E. (2018). Weakly or strongly nonlinear mesoscale dynamics close to the tropopause? *Journal of the Atmospheric Sciences*, *75*(4), 1215–1229. doi: 10.1175/jas-d-17-0063.1

Lindborg, E. (1999). Can the atmospheric kinetic energy spectrum be explained by two-dimensional turbulence? *Journal of Fluid Mechanics*, *388*, 259–288. doi: 10.1017/s0022112099004851

Morice, C. P., Kennedy, J. J., Rayner, N. A., & Jones, P. D. (2012). Quantifying uncertainties in global and regional temperature change using an ensemble of observational estimates: The HadCRUT4 data set. *Journal of Geophysical Research: Atmospheres*, *117*(D8). doi: 10.1029/2011jd017187

Moss, A. C., Wright, C. J., & Mitchell, N. J. (2016). Does the madden-julian oscillation modulate stratospheric gravity waves? *Geophysical Research Letters*, *43*(8), 3973–3981. doi: 10.1002/2016gl068498

Murgatroyd, R. J., & Singleton, F. (1961). Possible meridional circulations in the stratosphere and mesosphere. *Quarterly Journal of the Royal Meteorological Society*, *87*(372), 125–135. doi: 10.1002/qj.49708737202

Namboothiri, S. P., Jiang, J. H., Kishore, P., Igarashi, K., Ao, C. O., & Romans, L. J. (2008). CHAMP observations of global gravity wave fields in the troposphere and stratosphere. *Journal of Geophysical Research*, *113*(D7). doi: 10.1029/2007jd008912

Ogi, M., Yamazaki, K., & Tachibana, Y. (2004). The summertime annular mode in the northern hemisphere and its linkage to the winter mode. *Journal of Geophysical Research*, *109*(D20). doi: 10.1029/2004jd004514

Plougonven, R., Hertzog, A., & Guez, L. (2012). Gravity waves over antarctica and the southern ocean: consistent momentum fluxes in mesoscale simulations and stratospheric balloon observations. *Quarterly Journal of the Royal Meteorological Society*, *139*(670), 101–118. doi: 10.1002/qj.1965

Plougonven, R., Teitelbaum, H., & Zeitlin, V. (2003). Inertia gravity wave generation by the tropospheric midlatitude jet as given by the Fronts and Atlantic Storm-Track Experiment radio soundings. *Journal of Geophysical Research: Atmospheres*, *108*(D21). doi: 10.1029/2003jd003535

Scott, R. K., Cammas, J.-P., Mascart, P., & Stolle, C. (2001). Stratospheric filamentation into the upper tropical troposphere. *Journal of Geophysical Research: Atmospheres*, *106*(D11), 11835–11848. doi: 10.1029/2001jd900049

Skamarock, W. C. (2004). Evaluating mesoscale NWP models using kinetic energy spectra. *Monthly Weather Review*, *132*(12), 3019–3032. doi: 10.1175/mwr2830.1

Trenberth, K. E., & Stepaniak, D. P. (2001). Indices of El Niño Evolution. *Journal of Climate*, *14*(8), 1697-1701. doi: 10.1175/1520-0442(2001)014⟨1697:LIOENO⟩2.0.CO;2

Vaughan, G., & Worthington, R. M. (2007). Inertia-gravity waves observed by the UK MST radar. *Quarterly Journal of the Royal Meteorological Society*, *133*(S2), 179–188. doi: 10.1002/qj.142

Wang, L., & Geller, M. A. (2003). Morphology of gravity-wave energy as observed from 4 years (1998–2001) of high vertical resolution U.S. radiosonde data. *Journal of Geophysical Research*, *108*(D16), ACL 1–1–ACL 1–12. doi: 10.1029/2002jd002786

Wright, C. J., & Hindley, N. P. (2018). How well do stratospheric reanalyses reproduce high-resolution satellite temperature measurements? *Atmospheric Chemistry and Physics*, *18*(18), 13703–13731. doi: 10.5194/acp-18-13703-2018

Wright, C. J., Osprey, S. M., Barnett, J. J., Gray, L. J., & Gille, J. C. (2010). High Resolution Dynamics Limb Sounder measurements of gravity wave activity in the 2006 arctic stratosphere. *Journal of Geophysical Research*, *115*(D2). doi: 10.1029/2009jd011858

Wright, C. J., Osprey, S. M., & Gille, J. C. (2015). Global distributions of overlapping gravity waves in HIRDLS data. *Atmospheric Chemistry and Physics*, *15*(14), 8459–8477. doi: 10.5194/acp-15-8459-2015

Wright, C. J., Scott, R. B., Arbic, B. K., & Furnival, D. F. (2012). Bottom dissipation of subinertial currents at the atlantic zonal boundaries. *Journal of Geophysical Research: Oceans*, *117*(C3). doi: 10.1029/2011jc007702

Wright, C. J., Scott, R. B., Furnival, D., Ailliot, P., & Vermet, F. (2013, February). Global observations of ocean-bottom subinertial current dissipation. *Journal of Physical Oceanography*, *43*(2), 402–417. Retrieved from `https://doi.org/10.1175/jpo-d-12-082.1` doi: 10.1175/jpo-d-12-082.1

Figure 1.

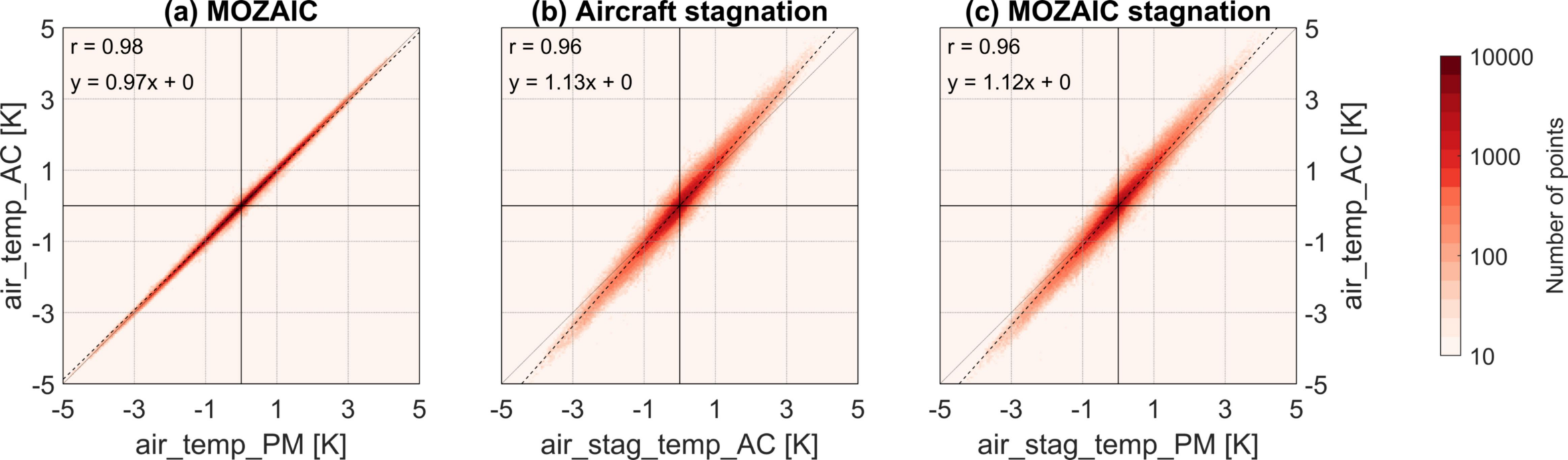
(a) MOZAIC
r = 0.98
y = 0.97x + 0
air_temp_AC [K]
air_temp_PM [K]
(b) Aircraft stagnation
r = 0.96
y = 1.13x + 0
air_stag_temp_AC [K]
(c) MOZAIC stagnation
r = 0.96
y = 1.12x + 0
air_stag_temp_PM [K]
5
3
1
-1
-3
-5
10000
1000
100
10
Number of points

Figure 2.

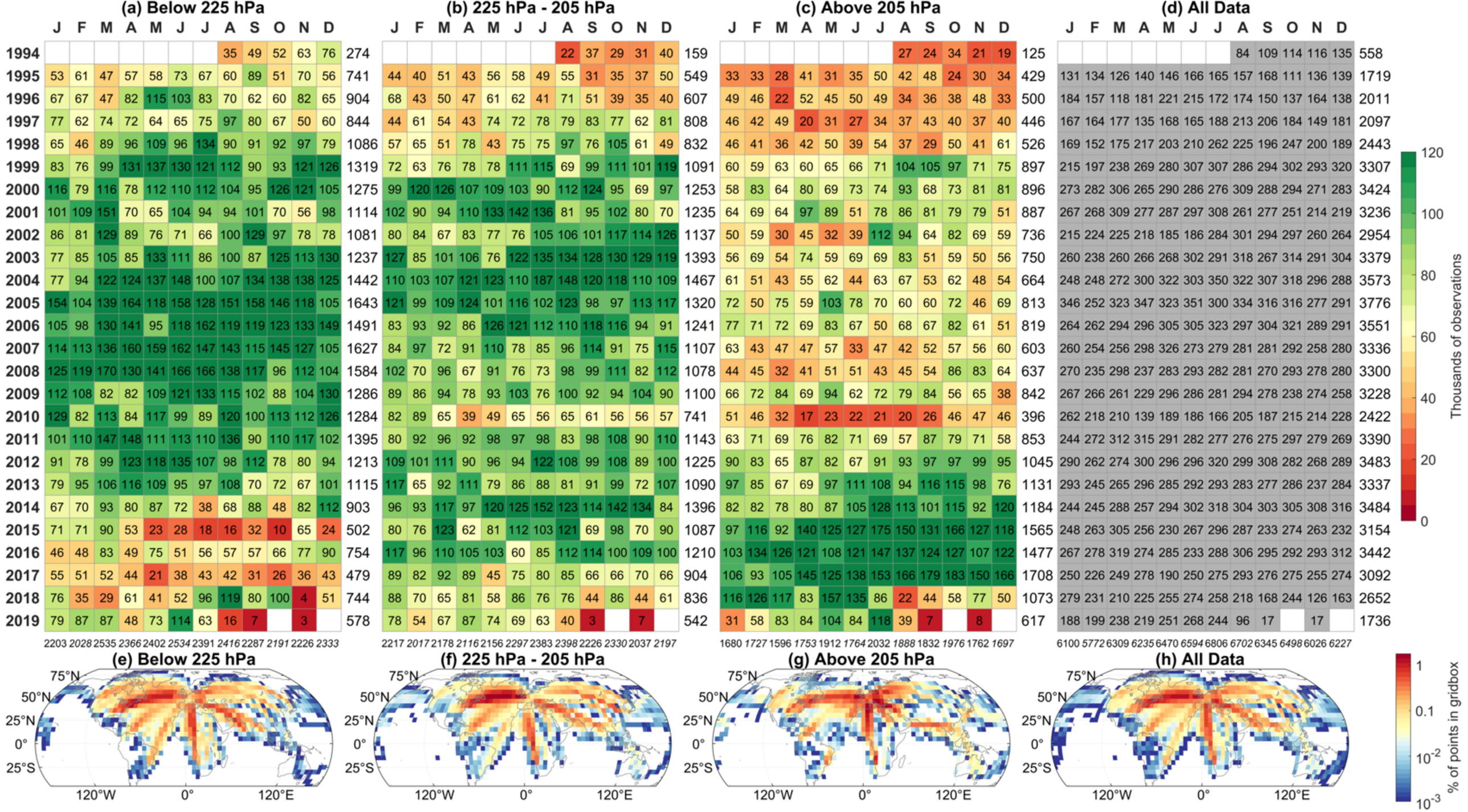
(a) Below 225 hPa
(b) 225 hPa - 205 hPa
(c) Above 205 hPa
(d) All Data
J F M A M J J A S O N D
1994 35 49 52 63 76 274 22 37 29 31 40 159 27 24 34 21 19 125 84 109 114 116 135 558
1995 53 61 47 57 58 73 67 60 89 51 70 56 741 44 40 51 43 56 58 49 55 31 35 37 50 549 33 33 28 41 31 35 50 42 48 24 30 34 429 131 134 126 140 146 166 165 157 168 111 136 139 1719
1996 67 67 47 82 115 103 83 70 62 60 82 65 904 68 43 50 47 61 62 41 71 51 39 35 40 607 49 46 22 52 45 50 49 34 36 38 48 33 500 184 157 118 181 221 215 172 174 150 137 164 138 2011
1997 77 62 74 72 64 65 75 97 80 67 50 60 844 44 61 54 43 74 72 78 79 83 77 62 81 808 46 42 49 20 31 27 34 37 43 40 37 40 446 167 164 177 135 168 165 188 213 206 184 149 181 2097
1998 65 46 89 96 109 96 134 90 91 92 97 79 1086 57 65 51 78 43 75 75 97 76 105 61 49 832 46 41 36 42 50 39 54 37 29 50 41 61 526 169 152 175 217 203 210 262 225 196 247 200 189 2443
1999 83 76 99 131 137 130 121 112 90 93 121 126 1319 72 63 76 78 78 111 115 69 99 111 101 119 1091 60 59 63 60 65 66 71 104 105 97 71 75 897 215 197 238 269 280 307 307 286 294 302 293 320 3307
2000 116 79 116 78 112 110 112 104 95 126 121 105 1275 99 120 126 107 109 103 90 112 124 95 69 97 1253 58 83 64 80 69 73 74 93 68 73 81 81 896 273 282 306 265 290 286 276 309 288 294 271 283 3424
2001 101 109 151 70 65 104 94 94 101 70 56 98 1114 102 90 94 110 133 142 136 81 95 102 80 70 1235 64 69 64 97 89 51 78 86 81 79 79 51 887 267 268 309 277 287 297 308 261 277 251 214 219 3236
2002 86 81 129 89 76 71 66 100 129 97 78 78 1081 80 84 67 83 77 76 105 106 101 117 114 126 1137 50 59 30 45 32 39 112 94 64 82 69 59 736 215 224 225 218 185 186 284 301 294 297 260 264 2954
2003 77 85 105 85 133 111 86 100 87 125 113 130 1237 127 85 101 106 76 122 135 134 128 130 129 119 1393 56 69 54 74 59 69 69 83 51 59 50 56 750 260 238 260 266 268 302 291 318 267 314 291 304 3379
2004 77 94 122 124 137 148 100 107 134 138 138 125 1442 110 103 107 121 123 110 187 148 120 118 110 109 1467 61 51 43 55 62 44 63 67 53 62 48 54 664 248 248 272 300 322 303 350 322 307 318 296 288 3573
2005 154 104 139 164 118 158 128 151 158 146 118 105 1643 121 99 109 124 101 116 102 123 98 97 113 117 1320 72 50 75 59 103 78 70 60 60 72 46 69 813 346 252 323 347 323 351 300 334 316 316 277 291 3776
2006 105 98 130 141 95 118 162 119 119 123 133 149 1491 83 93 92 86 126 121 112 110 118 116 94 91 1241 77 71 72 69 83 67 50 68 67 82 61 51 819 264 262 294 296 305 305 323 297 304 321 289 291 3551
2007 114 113 136 160 159 162 147 143 115 145 127 105 1627 84 97 72 91 110 78 85 96 114 91 75 115 1107 63 43 47 47 57 33 47 42 52 57 56 60 603 260 254 256 298 326 273 279 281 281 292 258 280 3336
2008 125 119 170 130 141 166 166 138 117 96 112 104 1584 102 70 96 67 91 76 73 98 99 111 82 112 1078 44 45 32 41 51 51 43 45 54 86 83 64 637 270 235 298 237 283 293 282 281 270 293 278 280 3300
2009 112 108 82 82 109 121 133 115 102 88 104 130 1286 89 86 94 78 93 103 76 100 92 94 104 90 1100 66 72 84 69 94 62 72 79 84 56 65 38 842 267 266 261 229 296 286 281 294 278 238 274 258 3228
2010 129 82 113 84 117 99 89 120 100 113 112 126 1284 82 89 65 39 49 65 56 65 61 56 56 57 741 51 46 32 17 23 22 21 20 26 46 47 46 396 262 218 210 139 189 186 166 205 187 215 214 228 2422
2011 101 110 147 148 111 113 110 136 90 110 117 102 1395 80 92 96 92 98 97 98 83 98 108 90 110 1143 63 71 69 76 82 71 69 57 87 79 71 58 853 244 272 312 315 291 282 277 276 275 297 279 269 3390
2012 91 78 99 123 118 135 107 98 112 78 80 94 1213 109 101 111 90 96 94 122 108 99 108 89 100 1225 90 83 65 87 82 67 91 93 97 97 99 95 1045 290 262 274 300 296 296 320 299 308 282 268 289 3483
2013 79 95 106 116 109 95 97 108 70 72 67 101 1115 117 65 92 111 79 86 88 81 91 99 72 107 1090 97 85 67 69 97 111 108 94 116 115 98 76 1131 293 245 265 296 285 292 293 283 277 286 237 284 3337
2014 67 70 93 80 87 72 38 68 88 48 82 112 903 96 93 117 97 120 125 152 123 114 142 134 84 1396 82 82 78 80 87 105 128 113 101 115 92 120 1184 244 245 288 257 294 302 318 304 303 305 308 316 3484
2015 71 71 90 53 23 28 18 16 32 10 65 24 502 80 76 123 62 81 112 103 121 69 98 70 90 1087 97 116 92 140 125 127 175 150 131 166 127 118 1565 248 263 305 256 230 267 296 287 233 274 263 232 3154
2016 46 48 83 49 75 51 56 57 57 66 77 90 754 117 96 110 105 103 60 85 112 114 100 109 100 1210 103 134 126 121 108 121 147 137 124 127 107 122 1477 267 278 319 274 285 233 288 306 295 292 293 312 3442
2017 55 51 52 44 21 38 43 42 31 26 36 43 479 89 82 92 89 45 75 80 85 66 66 70 66 904 106 93 105 145 125 138 153 166 179 183 150 166 1708 250 226 249 278 190 250 275 293 276 275 255 274 3092
2018 76 35 29 61 41 52 96 119 80 100 4 51 744 88 70 65 81 58 86 76 76 44 86 44 61 836 116 126 117 83 157 135 86 22 44 58 77 50 1073 279 231 210 225 255 274 258 218 168 244 126 163 2652
2019 79 87 87 48 73 114 63 16 7 3 578 78 54 67 87 74 69 63 40 3 7 542 31 58 83 84 104 84 118 39 7 8 617 188 199 238 219 251 268 244 96 17 17 1736
2203 2028 2535 2366 2402 2534 2391 2416 2287 2191 2226 2333
2217 2017 2178 2116 2156 2297 2383 2398 2226 2330 2037 2197
1680 1727 1596 1753 1912 1764 2032 1888 1832 1976 1762 1697
6100 5772 6309 6235 6470 6594 6806 6702 6345 6498 6026 6227
Thousands of observations
120
100
80
60
40
20
0
(e) Below 225 hPa
(f) 225 hPa - 205 hPa
(g) Above 205 hPa
(h) All Data
75°N
50°N
25°N
0°
25°S
120°W
0°
120°E
% of points in gridbox
1
0.1
10^{-2}
10^{-3}

Figure 3.

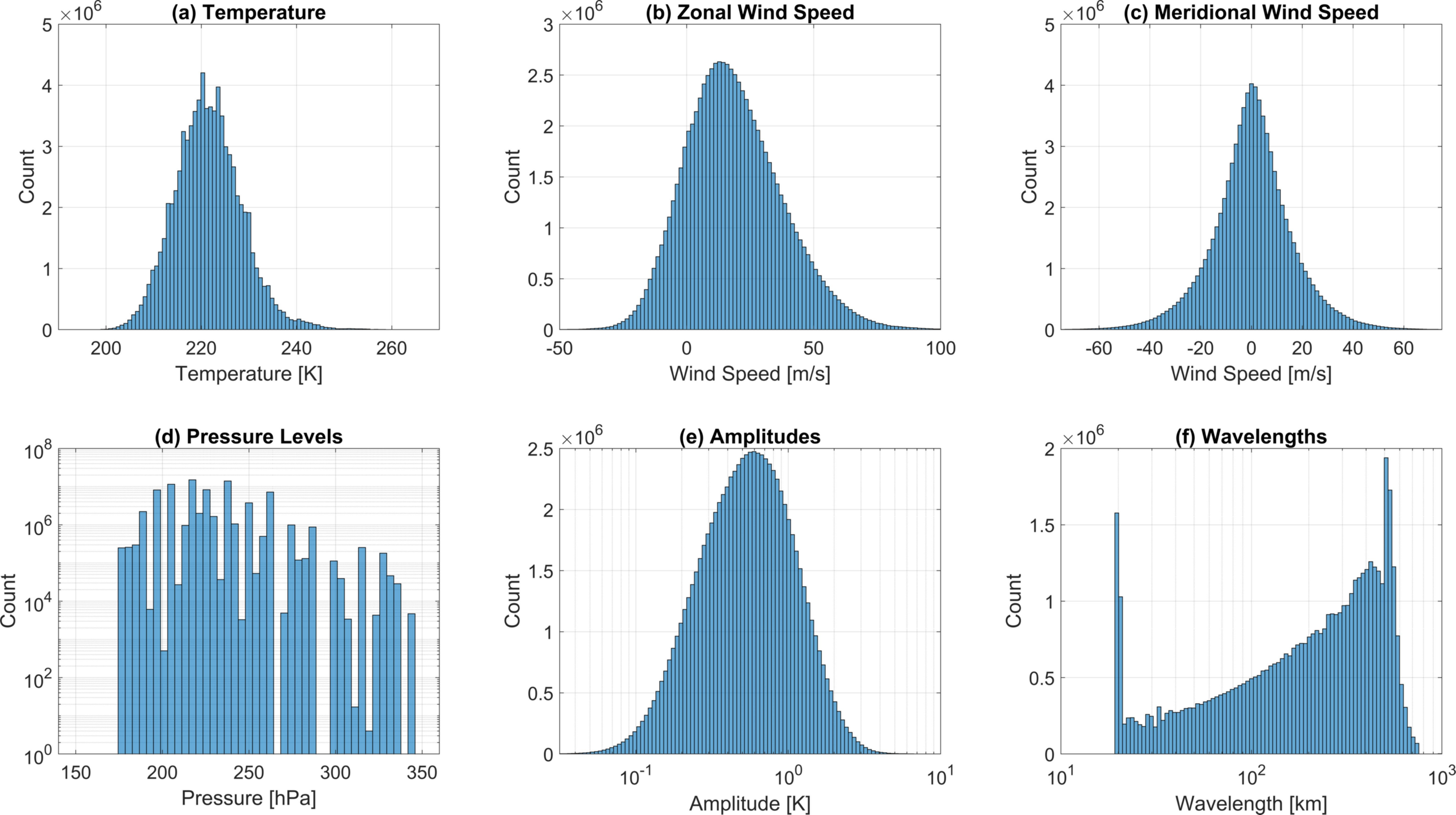
(a) Temperature
×10^6
Count
Temperature [K]
(b) Zonal Wind Speed
Wind Speed [m/s]
(c) Meridional Wind Speed
Wind Speed [m/s]
(d) Pressure Levels
Pressure [hPa]
(e) Amplitudes
Amplitude [K]
(f) Wavelengths
Wavelength [km]

Figure 4.

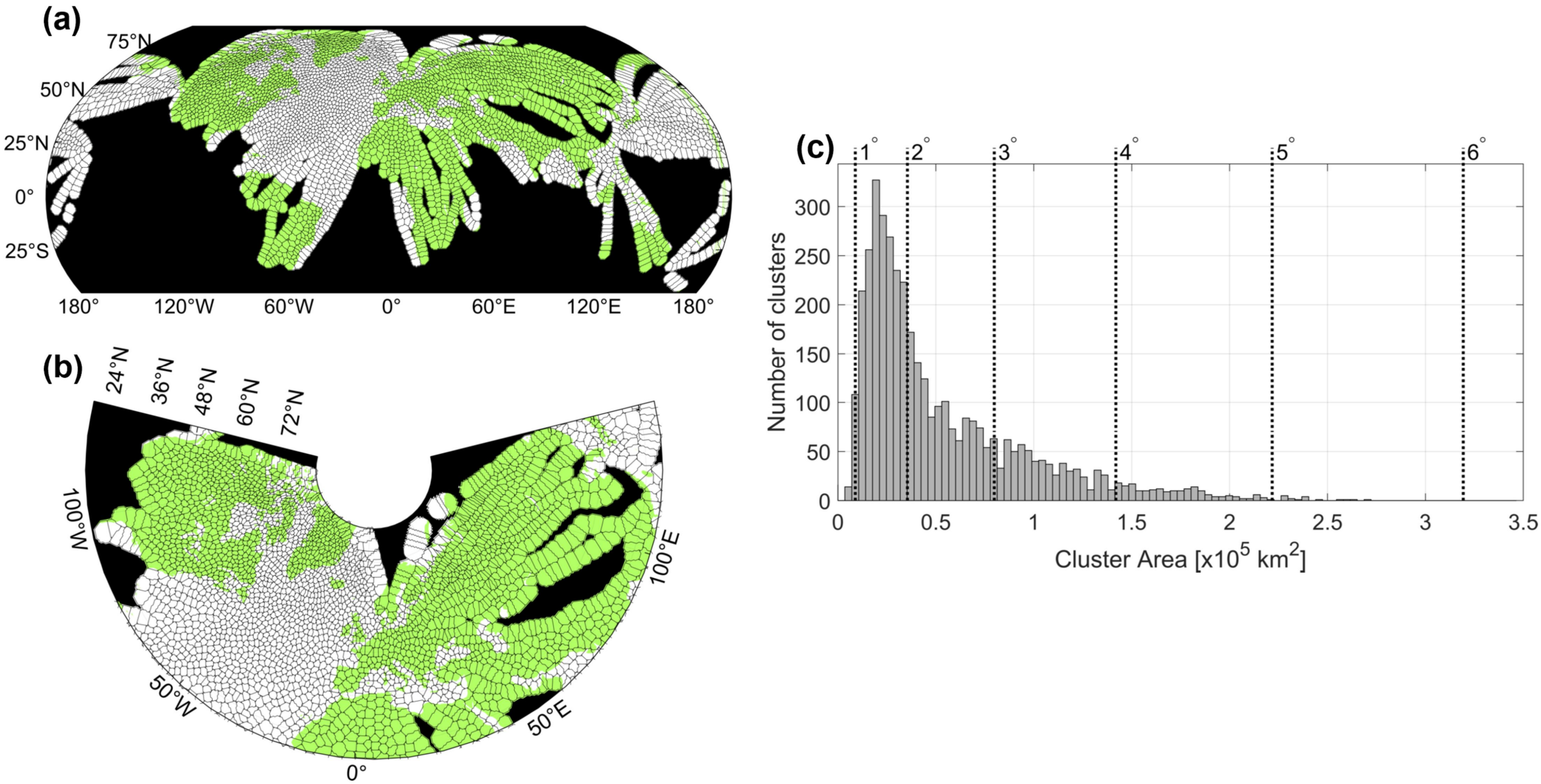
(a)
75°N
50°N
25°N
0°
25°S
180°
120°W
60°W
0°
60°E
120°E
180°
(b)
24°N
36°N
48°N
60°N
72°N
100°W
50°W
0°
50°E
100°E
(c)
1°
2°
3°
4°
5°
6°
Number of clusters
0
50
100
150
200
250
300
0
0.5
1
1.5
2
2.5
3
3.5
Cluster Area [x10^5 km^2]

Figure 5.

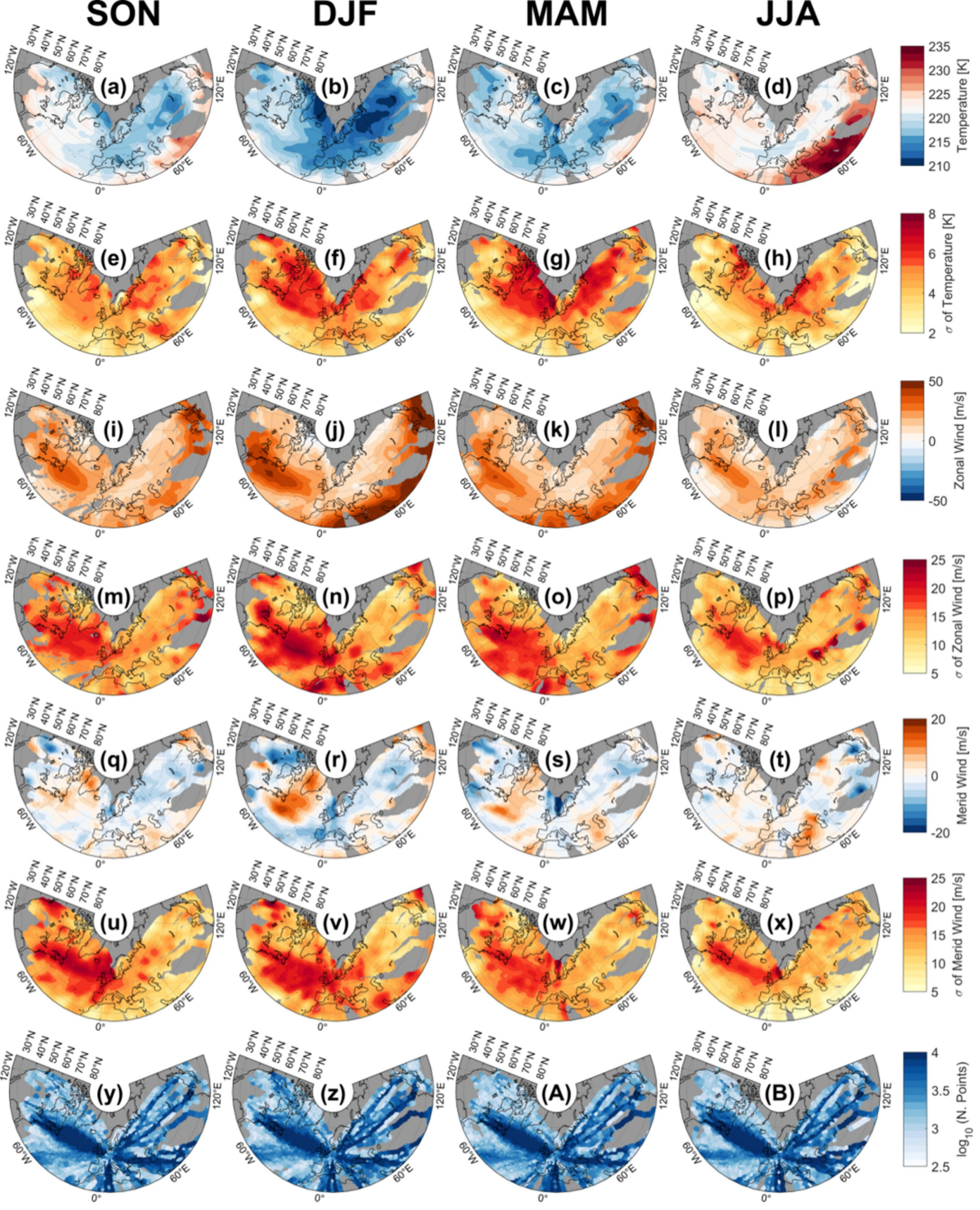
SON
DJF
MAM
JJA
(a)
(b)
(c)
(d)
(e)
(f)
(g)
(h)
(i)
(j)
(k)
(l)
(m)
(n)
(o)
(p)
(q)
(r)
(s)
(t)
(u)
(v)
(w)
(x)
(y)
(z)
(A)
(B)
30°N
40°N
50°N
60°N
70°N
80°N
120°W
120°E
60°W
60°E
0°
235
230
225
220
215
210
Temperature [K]
8
6
4
2
σ of Temperature [K]
50
0
-50
Zonal Wind [m/s]
25
20
15
10
5
σ of Zonal Wind [m/s]
20
0
-20
Merid Wind [m/s]
σ of Merid Wind [m/s]
4
3.5
3
2.5
log10 (N. Points)

Figure 6.

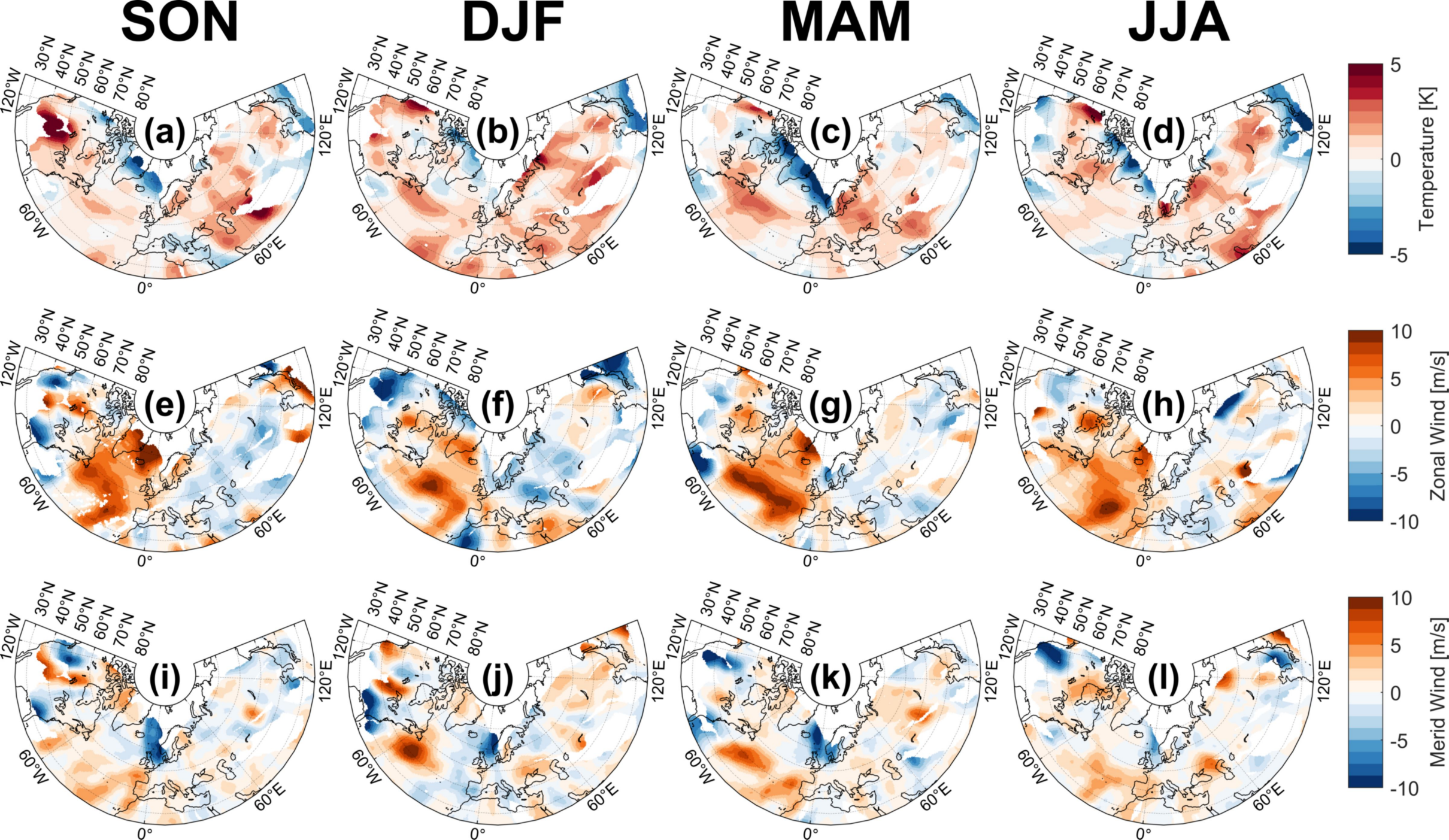
SON
DJF
MAM
JJA
(a)
(b)
(c)
(d)
(e)
(f)
(g)
(h)
(i)
(j)
(k)
(l)
30°N
40°N
50°N
60°N
70°N
80°N
120°W
60°W
0°
60°E
120°E
Temperature [K]
5
0
-5
Zonal Wind [m/s]
10
5
0
-5
-10
Merid Wind [m/s]
10
5
0
-5
-10

Figure 7.

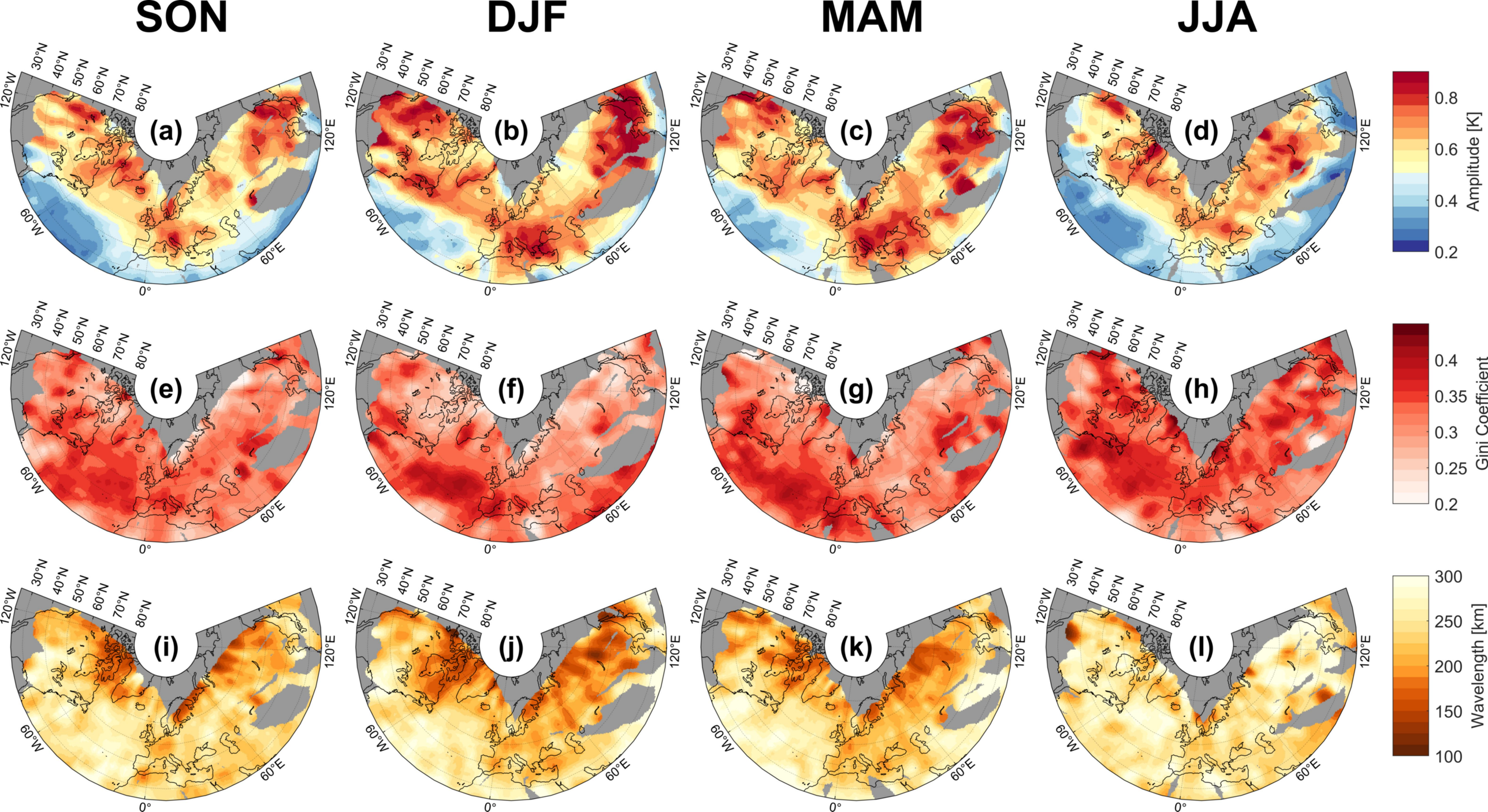
SON
DJF
MAM
JJA
(a)
(b)
(c)
(d)
(e)
(f)
(g)
(h)
(i)
(j)
(k)
(l)
120°W
30°N
40°N
50°N
60°N
70°N
80°N
120°E
60°W
60°E
0°
Amplitude [K]
0.8
0.6
0.4
0.2
Gini Coefficient
0.4
0.35
0.3
0.25
0.2
Wavelength [km]
300
250
200
150
100

Figure 8.

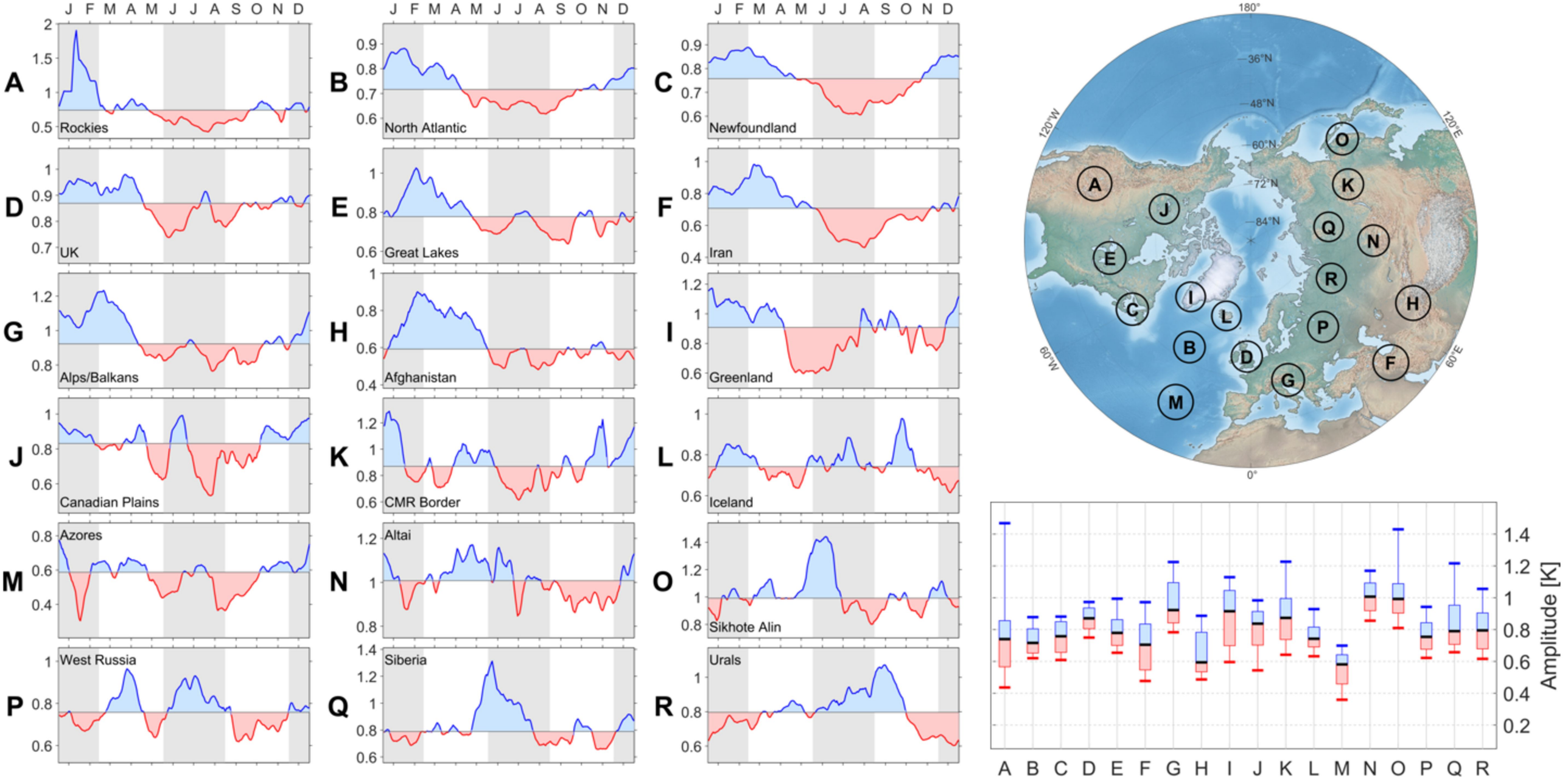
J F M A M J J A S O N D
A
Rockies
B
North Atlantic
C
Newfoundland
D
UK
E
Great Lakes
F
Iran
G
Alps/Balkans
H
Afghanistan
I
Greenland
J
Canadian Plains
K
CMR Border
L
Iceland
M
Azores
N
Altai
O
Sikhote Alin
P
West Russia
Q
Siberia
R
Urals
180°
36°N
48°N
60°N
72°N
84°N
120°W
120°E
60°W
60°E
0°
Amplitude [K]
A B C D E F G H I J K L M N O P Q R

Figure 9.

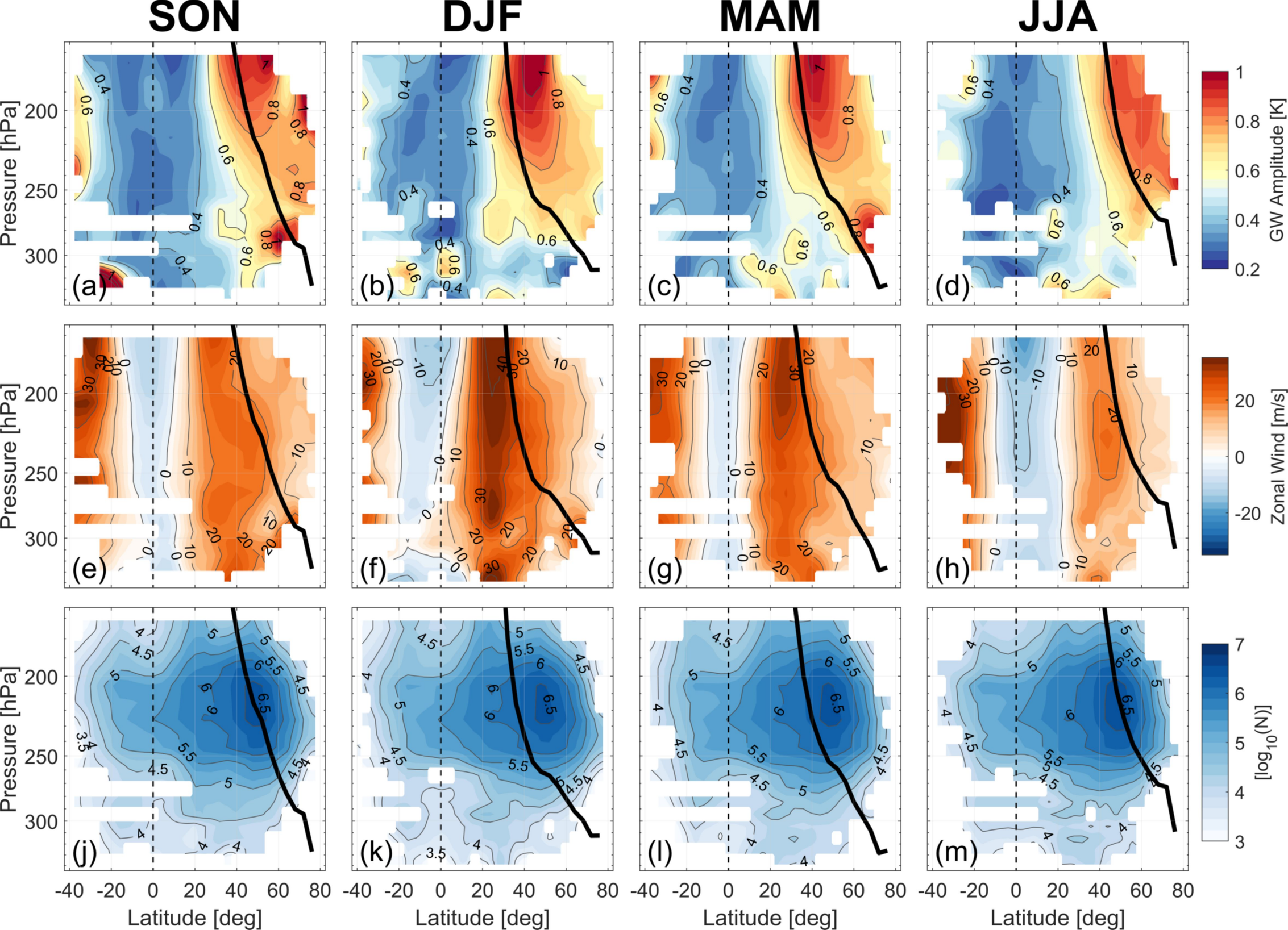
SON
DJF
MAM
JJA
Pressure [hPa]
200
250
300
(a)
(b)
(c)
(d)
(e)
(f)
(g)
(h)
(j)
(k)
(l)
(m)
GW Amplitude [K]
1
0.8
0.6
0.4
0.2
Zonal Wind [m/s]
20
0
-20
[log10(N)]
7
6
5
4
3
-40 -20 0 20 40 60 80
Latitude [deg]

Figure 10.

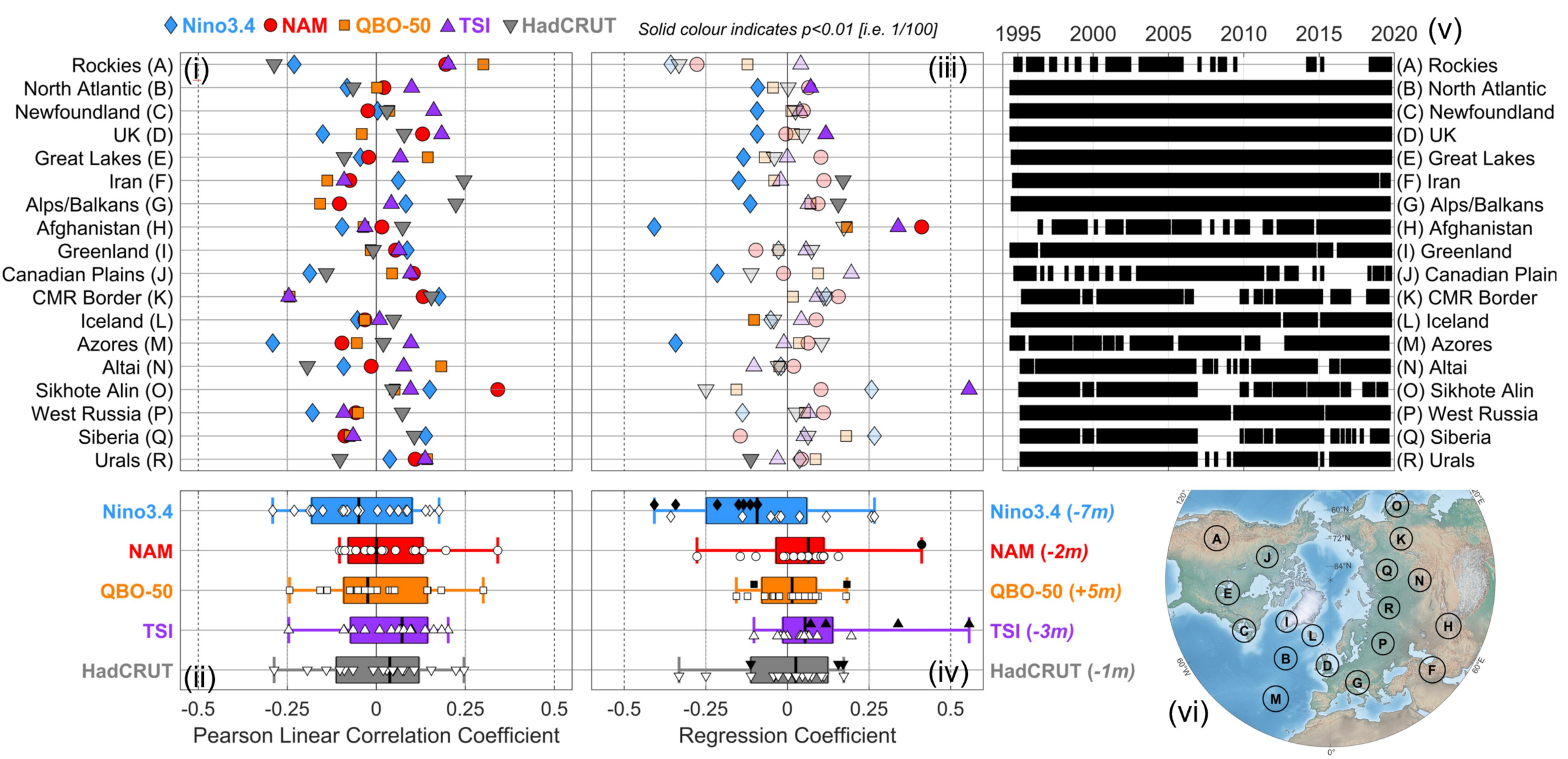
Nino3.4
NAM
QBO-50
TSI
HadCRUT
Solid colour indicates p<0.01 [i.e. 1/100]
(i)
(ii)
(iii)
(iv)
(v)
(vi)
Rockies (A)
North Atlantic (B)
Newfoundland (C)
UK (D)
Great Lakes (E)
Iran (F)
Alps/Balkans (G)
Afghanistan (H)
Greenland (I)
Canadian Plains (J)
CMR Border (K)
Iceland (L)
Azores (M)
Altai (N)
Sikhote Alin (O)
West Russia (P)
Siberia (Q)
Urals (R)
1995
2000
2005
2010
2015
2020
(A) Rockies
(B) North Atlantic
(C) Newfoundland
(D) UK
(E) Great Lakes
(F) Iran
(G) Alps/Balkans
(H) Afghanistan
(I) Greenland
(J) Canadian Plain
(K) CMR Border
(L) Iceland
(M) Azores
(N) Altai
(O) Sikhote Alin
(P) West Russia
(Q) Siberia
(R) Urals
-0.5
-0.25
0
0.25
0.5
Pearson Linear Correlation Coefficient
Regression Coefficient
Nino3.4 (-7m)
NAM (-2m)
QBO-50 (+5m)
TSI (-3m)
HadCRUT (-1m)
60°N
72°N
84°N
120°W
60°W
0°
60°E
120°E